A fictitious domain method for lithosphere-asthenosphere interaction: Application to periodic slab folding in the upper mantle

Nestor G. Cerpa, R. Hassani, M. Gerbault, J-Hervé Prévost

10.1002/2014GC005241

A fictitious domain method for lithosphere-asthenosphere interaction: Application to periodic slab folding in the upper mantle

Nestor G. Cerpa[1], Riad Hassani[1], Muriel Gerbault[1], and Jean-Herve Prévost[2]

[1]Géoazur, UMR 7329, CNRS, IRD, Observatoire de la Côte d'Azur, Université de Nice Sophia Antipolis, Valbonne, France, [2]Department of Civil and Environmental Engineering, Princeton University, Princeton, New Jersey, USA

Abstract We present a new approach for the lithosphere-asthenosphere interaction in subduction zones. The lithosphere is modeled as a Maxwell viscoelastic body sinking in the viscous asthenosphere. Both domains are discretized by the finite element method, and we use a staggered coupling method. The interaction is provided by a nonmatching interface method called the fictitious domain method. We describe a simplified formulation of this numerical technique and present 2-D examples and benchmarks. We aim at studying the effect of mantle viscosity on the cyclicity of slab folding at the 660 km depth transition zone. Such cyclicity has previously been shown to occur depending on the kinematics of both the overriding and subducting plates, in analog and numerical models that approximate the 660 km depth transition zone as an impenetrable barrier. Here we applied far-field plate velocities corresponding to those of the South-American and Nazca plates at present. Our models show that the viscosity of the asthenosphere impacts on folding cyclicity and consequently on the slab's dip as well as the stress regime of the overriding plate. Values of the mantle viscosity between 3 and 5 $\times$ 10^{20} Pa s are found to produce cycles similar to those reported for the Andes, which are of the order of 30–40 Myr (based on magmatism and sedimentological records). Moreover, we discuss the episodic development of horizontal subduction induced by cyclic folding and, hence, propose a new explanation for episodes of flat subduction under the South-American plate.

Key Points:

- Fluid solid coupling method
- Lithosphere asthenosphere interaction
- Periodic slab folding on the 660 km discontinuity

Correspondence to:
N. G. Cerpa,
nestor.cerpa@geoazur.unice.fr

Citation:
Cerpa, N. G., R. Hassani, M. Gerbault, and J. H. Prévost (2014), A fictitious domain method for lithosphere asthenosphere interaction: Application to periodic slab folding in the upper mantle, *Geochem. Geophys. Geosyst.*, *15*, 1852–1877, doi:10.1002/2014GC005241.

1. Introduction

Seismic tomography provides a present-day image of subducting plate geometries throughout the Earth's mantle [*Rubie and Van der Hilst*, 2001; *Fukao and Obayashi*, 2013]. Analytical studies have unraveled the primary driving forces and parameters that control such geometries [e.g., *Forsyth and Uyeda*, 1975], yet many variations remain unexplained. In order to fully understand the dynamics of subduction zones, their temporal evolution can only be tackled with numerical, analog, and statistical approaches. Current subduction zone data such as plates velocity, trench motion, back-arc deformation, and slab dip were gathered in order to reveal statistical correlations between these parameters [*Jarrard*, 1986; *Heuret and Lallemand*, 2005; *Lallemand et al.*, 2005]. *Heuret and Lallemand* [2005] found a general relationship between upper-plate velocity and back-arc deformation. Nevertheless, they pointed out a potential role of mantle flow in the relative motions between subducting and overriding plates, and the forces acting on them. Asthenospheric flow data being poorly constrained, modeling studies complement our understanding of asthenosphere-lithosphere interactions in subduction zones.

Without disregarding the importance of analog models, we focus here on numerical models. Such models are numerous and can be classified according to their main assumptions. Some consider a mantle convection approach, whereby the dynamic system is mainly controlled by slab-pull, which drives the sinking of the subducted slab deeper into the mantle [*Stegman et al.*, 2006; *Morra and Regenauer-Lieb*, 2006; *Capitanio et al.*, 2010; *Stegman et al.*, 2010; *Li and Ribe*, 2012]. Others consider a plate tectonic approach, whereby kinetic conditions constrain lithospheric displacements [*Christensen*, 1996; *Shemenda*, 1993; *Čížková et al.*, 2002; *Zlotnik et al.*, 2007; *Gibert et al.*, 2012]. Our approach for modeling the dynamics of subduction zones belongs to this second class and is similar to that of *Hassani et al.* [1997] and *Gibert et al.* [2012]. Boundary kinematic conditions are imposed at the far edges of the plates, and a density contrast between the lithosphere and the underneath mantle generates the slab-pull. The interaction between the subducting and the overriding plates is modeled, as well as the interaction with an impenetrable discontinuity at 660 km depth separating the upper and lower mantle. Nonetheless, *Hassani et al.* [1997] and *Gibert et al.* [2012] have not taken into account the mantle

viscous drag because of the numerical difficulties in coupling the physics of two rheologically different deformable bodies. The present study was motivated by the aim to test the role of mantle viscosity on their results.

Subduction dynamics, like other geodynamic problems, can be viewed as a competent body embedded in a more deformable medium. From a mechanical point of view, modeling this solid-fluid interaction requires coupling of two physically distinct domains. Usually this kind of problem, which is widespread in many fields (industry, biomedical research, civil engineering, etc.), is solved with common discretization methods, such as the Finite Element Method (FEM), Finite Differences, or Finites Volumes, which allow to solve partial differential equations (PDE) in an approximated form.

Intuitively, we could consider the exact discretization of both domains in order to solve the interaction problem, i.e., we have to fit as well as possible the shape of the interface between the two domains. This strategy was used in *Bonnardot et al.* [2008a] for the lithosphere-asthenosphere interaction, where the fluid and the solid domains are exactly meshed and their joined discrete problem is solved with FEM. As a consequence, the solid's displacements (and deformation) lead to fluid mesh distortion, and a remeshing technique is needed. This last procedure is computationally expensive. Moreover, in a subduction context, the lithosphere is submitted to large deformation and can acquire a complex geometry [e.g., *Gibert et al.*, 2012].

To alleviate the precise meshing of complex geometries, numerical modelers have developed the so-called Fictitious Domain Methods (FDM), also known as "domain embedding methods," whose name was introduced by *Saul'ev* [1963]. The first application of these methods in fluid-solids problems was credited to *Peskin* [1972] who modeled heart blood flow. The main idea is to extend the initial problem to a bigger (and simpler) domain, aiming for a simpler mesh to solve the given PDE discretized problem. Generally, the initial domain is "embedded" in a Cartesian grid. Many FDM have been developed to solve all types of physical problems. In fluid modeling (Stokes or Navier-Stokes), one can quote the immersed boundary method [*Peskin*, 1972; *Lai and Peskin*, 2000], the immersed interface method [*LeVeque and Li*, 1994], the fat boundary method [*Maury*, 2001], the Lagrange multiplier fictitious domain [*Glowinski et al.*, 1995], and the distributed Lagrange multiplier method [*Glowinski et al.*, 1999]. To our knowledge, these kinds of solid-fluid coupling methods have not yet been used in geodynamics. Thus, starting from the Lagrange multiplier fictitious domain, we propose here a simple formulation of a nonmatching interface method.

We developed this new fluid-solid coupling method, using the finite element code ADELI for the solid problem [*Hassani et al.*, 1997; *Chéry et al.*, 2001] and another standard FEM solver for viscous flow, in order to explore the influence of mantle viscosity on subduction cyclicity. Such cyclicity was revealed by numerical [*Gibert et al.*, 2012] and analog [*Heuret et al.*, 2007] models to depend on a specific relationship between plate kinematics, e.g., far-field velocities of the overriding and subducting plates. Other analog and numerical models simulating freely sinking plates have also produced slab folding on the 660 discontinuity, depending on plate-mantle viscosity and thickness ratios [*Schellart*, 2008] or on the Stokes buoyancy and effective viscous rigidity of plates [*Stegman et al.*, 2010]. In the present study, we only aim at validating our method and at testing the effect of mantle viscosity on the results obtained by *Gibert et al.* [2012], for a given set of plate density, rheology, and thickness. The assessment of all rheological parameters and boundary conditions that control the dynamics of subduction zones remains out of our present scope.

This paper is structured as follows. First we recall the mechanical and numerical formulations of both the solid and the fluid modeling approaches. We detail in section 3 the coupling problem in continuous and discrete terms and present our new simplified fictitious domain method. In section 4, we present some benchmarks and examples. Then, in section 5, we present our parametric study of the effect of mantle viscosity on subduction cyclicity taking as example the kinematic conditions corresponding to the Andes. In section 6, we briefly discuss our results with respect to "free subduction" scaling analyses. We propose that subduction cyclicity may explain repeated episodes of flat subduction observed along the Andes and how it may also potentially retroact on far-field plate motion. Finally, we present our conclusions and prospects for future work.

2. Mechanical Modeling and Numerical Formulation

As in *Morra and Regenauer-Lieb* [2006] and *Bonnardot et al.* [2008b], the lithosphere-asthenosphere system is viewed as a solid-fluid interaction problem where, for reasonable viscosity contrasts, the lithospheric plates behave as solid bodies which are partially or totally immersed in a viscous fluid, namely, the

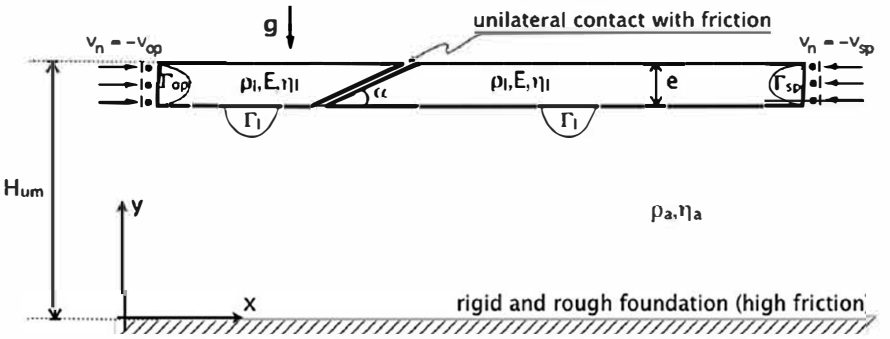

Figure 1. Physical model at initial time with boundary conditions on the solid. The upper mantle lower mantle boundary is modeled as an impermeable barrier on which the slab will anchor with a sufficiently high friction. Plate boundary velocities are expressed in reference to this bottom boundary, and positive values of v_{op} and v_{sp} correspond to trenchward motion.

asthenospheric mantle. In this first section, we provide the governing equations which are used to model the mechanical evolution of each solid and fluid domain and how both interact. We will further detail the fluid-solid interaction in section 3, which is the technical novelty of the present paper.

2.1. Governing Equations

2.1.1. Solid Lithospheric Plates

The governing equations for the quasistatic evolution of lithospheric plates occupying a physical domain $\Omega \subset \mathbb{R}^2$ are

$$\begin{cases} \mathbf{div}\,\boldsymbol{\sigma} + \rho_l \boldsymbol{g} = \mathbf{0} & \text{in } \Omega_l, \\ \dfrac{D\boldsymbol{\sigma}}{Dt} = \mathcal{M}(\boldsymbol{\sigma}, \boldsymbol{d}) & \text{in } \Omega_l, \end{cases} \tag{1}$$

where σ is the Cauchy stress field, $\boldsymbol{g}$ is the vector of gravity acceleration, ρ_l is lithospheric density, $\boldsymbol{d}$ $\frac{1}{2}(\nabla \dot{\boldsymbol{u}} + \nabla \dot{\boldsymbol{u}}^T)$ is the Eulerian strain rate tensor, and $\dot{\boldsymbol{u}}$ the velocity field. $D\boldsymbol{\sigma}/Dt$ stands for an objective time derivative and $\mathcal{M}$ represents a general constitutive law. We assume in this study a simple elastic or viscoelastic Maxwell behavior

$$\mathcal{M}(\boldsymbol{\sigma}, \boldsymbol{d}) = 2G\boldsymbol{d} + \lambda\, \mathrm{tr}\boldsymbol{d}\boldsymbol{I} \quad \frac{G}{\eta}\mathbf{dev}\boldsymbol{\sigma} \tag{2}$$

where tr and **dev** are, respectively, the trace and deviatoric parts of a second-order tensor, $\boldsymbol{I}$ is the identity tensor, λ and G are the Lamé parameters, and η is the viscosity coefficient.

Moreover, plate-plate and plate-rigid foundation interactions are modeled with the following conditions:

$$\begin{cases} \delta\dot{u}_n \leq 0\,,\ \sigma_n \leq 0\,,\ \delta\dot{u}_n\sigma_n \quad 0 & \text{on } \Gamma_c, \\ |\sigma_t| \leq \quad \mu\sigma_n \text{ if } \delta\dot{u}_t \quad 0 & \text{on } \Gamma_c, \\ \sigma_t \quad \mu\sigma_n \dfrac{\delta\dot{u}_t}{|\delta\dot{u}_t|} \text{ if } \delta\dot{u}_t \ / \ 0 & \text{on } \Gamma_c, \end{cases} \tag{3}$$

where $\delta\dot{u}_n$ and $\delta\dot{u}_t$ are, respectively, the normal and tangential components of the relative velocity between two points in contact and μ is the friction coefficient. The normal components on the contact interface Γ_c are computed according to the outward normal vector. The first line of the equation (3) corresponds to the Signorini relations (no interpenetration, no attraction, and complementary condition) while the two remaining lines describe the Coulomb friction law. In addition, boundary conditions are imposed as velocity or stress components on parts of the solid domain boundary $\partial\Omega_l$. Figure 1 summarizes the solid model.

2.1.2. Fluid Asthenospheric Mantle

The stationary Stokes problem

$$\begin{cases} \mathbf{div}\,\boldsymbol{\tau} \quad \nabla p + \rho_a \boldsymbol{g} = \mathbf{0} & \text{in } \Omega_a, \\ \mathbf{div}\,\boldsymbol{v} = 0 & \text{in } \Omega_a, \end{cases} \tag{4}$$

is used to compute, at a given time t, the velocity field $\boldsymbol{v}$, the pressure p, and the viscous stress $\tau = \eta_a(\nabla \boldsymbol{v} + \nabla \boldsymbol{v}^T)$ in the fluid domain Ω_a, knowing the viscosity η_a, the density ρ_a, and a set of boundary conditions. The latter are expressed as velocity or stress components on a portion of the boundary of the fluid domain $\partial\Omega_a$.

2.1.3. Solid-Fluid Interaction

The continuity of the traction vector is required (action-reaction principle), on the interface Γ_{la} shared by the solid (lithosphere) and by the fluid (asthenosphere). Because of the viscosity, the fluid and the solid are perfectly glued to each other, which also implies the continuity of the velocity field on Γ_{la}

$$\begin{cases} \boldsymbol{v} = \dot{\boldsymbol{u}} & \text{on } \Gamma_{la}, \\ (\tau - p\boldsymbol{I}) \cdot \boldsymbol{n} = \boldsymbol{\sigma} \cdot \boldsymbol{n} & \text{on } \Gamma_{la}, \end{cases} \tag{5}$$

The application of our physical model to subduction systems presents the following restrictions, which are planned to be tackled in future work:

Viscosity and density remain constant in time, since thermal effects are ignored (as well as phase transitions). Consequently, our targeted applications are at the moment only valid for subductions zones that are fast enough compared to their thermal diffusion time scale. Viscosity and density also remain constant or piecewise constant in space since matter is not advected.

The upper-lower mantle interface at 660 km depth is modeled as an impenetrable barrier. The mechanism of slab penetration into the lower mantle is thus ignored.

2.2. Numerical Formulation

2.2.1. Solid Lithospheric Plates

An approximate solution to the continuous problem (1–3) is computed using the Galerkin finite element code ADELI. ADELI has been used in numerous geodynamical applications, for processes at the crustal scale [e.g., *Huc et al.*, 1998; *Got et al.*, 2008] as well as at the lithospheric scale [e.g., *Hassani et al.*, 1997; *Chéry et al.*, 2001; *Bonnardot et al.*, 2008b]. This code belongs to the FLAC family of codes [*Cundall and Board*, 1988; *Poliakov and Podladchikov*, 1992] and is based on the dynamic relaxation method.

In order to describe in section 3, our strategy to model the solid-fluid interaction, here we recall the time-discretization of the equilibrium equation (1) used in ADELI. More details about this code, in two and in three dimensions, can be found in *Hassani et al.* [1997] and *Chéry et al.* [2001].

The finite element approximation of the quasistatic equilibrium equation (1) leads to a set of algebraic nonlinear equations of the form

$$\boldsymbol{F}_{int}(\dot{\boldsymbol{U}}_{qs}, t) + \boldsymbol{F}_{ext}(\dot{\boldsymbol{U}}_{qs}, t) = 0 \tag{6}$$

where $\boldsymbol{F}_{int}$, $\boldsymbol{F}_{ext}$, and $\dot{\boldsymbol{U}}_{qs}$, vectors in $\mathbb{R}^{2N_l}$ (with N_l the number of nodes in the mesh of Ω_l), are internal forces, external forces, and nodal velocities, respectively. In the dynamic relaxation method [e.g., *Underwood*, 1983; *Cundall and Board*, 1988], the quasistatic solution $\dot{\boldsymbol{U}}_{qs}$ is approximated by the solution $\dot{\boldsymbol{U}}$ of a pseudodynamic problem by introducing a user-defined mass matrix $\boldsymbol{M}$, an acceleration vector $\ddot{\boldsymbol{U}}$, and a damping force vector $\boldsymbol{C}$. The discrete problem becomes

$$\boldsymbol{F}_{int}(\dot{\boldsymbol{U}}, t) + \boldsymbol{F}_{ext}(\dot{\boldsymbol{U}}, t) = \boldsymbol{M}\ddot{\boldsymbol{U}} + \boldsymbol{C} \tag{7}$$

Thus, when the acceleration and the damping force become negligible compared to the extemal and the internal forces, the quasistatic solution is reached [*Cundall*, 1988]. In addition, this method is coupled with an explicit time marching scheme

$$\begin{aligned} \ddot{\boldsymbol{U}}^{n+1} &= \boldsymbol{M}^{-1}[\boldsymbol{F}^n_{\cdot\cdot} + \boldsymbol{F}^n_{\cdot\cdot} - \boldsymbol{C}^n] \\ \dot{\boldsymbol{U}}^{n+1/2} &= \dot{\boldsymbol{U}}^{n-1/2} + \Delta t \ddot{\boldsymbol{U}}^{n+1} \\ \boldsymbol{U}^{n+1} &= \boldsymbol{U}^n + \Delta t \dot{\boldsymbol{U}}^{n+1/2} \end{aligned} \tag{8}$$

where $\ddot{\boldsymbol{U}}^{n+1}$ and $\boldsymbol{U}^{n+1}$ are the nodal acceleration and displacement vectors at time $t^{n+1} = t^n + \Delta t$, respectively, Δt is the time step, $\boldsymbol{M}^{-1}$ is the inverse mass matrix, $\boldsymbol{F}^n_{int}$ and $\boldsymbol{F}^n_{ext}$ are, respectively, the internal and external forces computed at t^n, and $\dot{\boldsymbol{U}}^{n+1/2}$ is the nodal velocities vector evaluated at time $t^{n+1/2} = t^n + \frac{1}{2}\Delta t$.

The term $\boldsymbol{C}$ damps the dynamic solution and enforces the convergence toward the quasistatic solution. It is chosen proportional to the out-of-forces balance, and it must thus vanish at the quasistatic equilibrium

$$C_j^n = \alpha_d |(F_{int}^n)_j + (F_{ext}^n)_j| \frac{(\dot{U}^n)_j}{|(\dot{U}^n)_j|} \tag{9}$$

for $j \quad 1, 2, \cdots, 2N_l$ and $\alpha_d \in]0, 1]$. In practice, $\alpha_d \quad 0.5$ or $\alpha_d \quad 0.8$ appear to be suitable values [see *Cundall*, 1988].

2.2.2. Fluid Asthenospheric Mantle

With regards to the classical stationary Stokes problem (4), the Galerkin finite element method with equal-order interpolant for both velocity and pressure is used. Hence, a stabilized technique based on polynomial pressure projections [*Dohrmann and Bochev*, 2004; *Burstedde et al.*, 2009] is needed. The fluid domain Ω_a is covered by a triangular or quadrilateral mesh of N_a nodes. The resulting discrete system is of the form

$$\boldsymbol{A}\begin{pmatrix} \boldsymbol{V} \\ \boldsymbol{P} \end{pmatrix} = \begin{pmatrix} \boldsymbol{F} \\ 0 \end{pmatrix}, \tag{10}$$

with $\boldsymbol{V} \in \mathbb{R}^{2N_a}$ the nodal velocities vector, $\boldsymbol{P} \in \mathbb{R}^{N_a}$ the nodal pressures vector, $\boldsymbol{F} \in \mathbb{R}^{2N_a}$ the nodal external forces, and $\boldsymbol{A}$ a symmetric $3N_a \times 3N_a$ matrix. Referring to subsequent sections, we can formally express the nodal velocities vector as the solution of a linear system of the type

$$\boldsymbol{KV} = \boldsymbol{F}_0. \tag{11}$$

3. Solid-Fluid Coupling: A Fictitious Domain Method

Modeling the interaction of a deformable structure moving in a fluid presents a number of challenging numerical problems. Among them is the way in which to follow the interface Γ_{la} which separates the solid and the fluid domains, and the resulting change in geometry of the fluid domain.

A first option consists in remeshing the fluid domain and was adopted by *Bonnardot et al.* [2008a]. However, this approach is arduous to implement, computationally time consuming, and laborious to deal with when the shape of the fluid domain becomes complex, especially in three dimensions. To alleviate meshing or remeshing efforts of complex domains, the Fictitious Domain Method (FDM) has been implemented in many fields for solving the interaction between two bodies of different physical behavior. FDM had initially been developed for the application of boundary conditions on geometrically complex boundaries [*Saul'ev*, 1963], and in our case, this type of method is also useful to solve the fluid problem on a Cartesian grid.

In the first of the two following subsections, we describe the general formulation of a simplified variation of FDM that we implemented. Then, we detail the numerical strategy adopted to interlock fluid and solid calculations in a stable manner.

3.1. General Formulation

To describe the Fictitious Domain Method (FDM), let us consider a simple linear problem where a scalar physical field v is sought in a domain Ω_a presenting a hole or an inclusion Ω_i of any shape (below we will also name it an obstacle). We name Γ_{ia} the boundary of the hole and Γ the external boundary of Ω_a (see Figure 2a). Assuming that the value of v is prescribed on Γ_{ia} and Γ, $\mathcal{L}$ is a given linear differential operator, and f is a known function, the linear problem is written

$$\begin{cases} \mathcal{L}(v) = f & \text{in } \Omega_a, \\ v = v_0 & \text{on } \Gamma, \\ v = v_{ia} & \text{on } \Gamma_{ia}. \end{cases} \tag{12}$$

In the standard finite element approach, the boundary condition on Γ_{ia} requires to define a mesh of Ω_a that matches as best as possible the shape of the obstacle. The main idea of the fictitious domain method is to extend the problem into a geometrically less complex domain $\Omega \quad \Omega_a \cup \Omega_i$ and to enforce the Dirichlet condition $v \quad v_{ia}$ on Γ_{ia} by introducing some source terms in (12) (see Figure 2b).

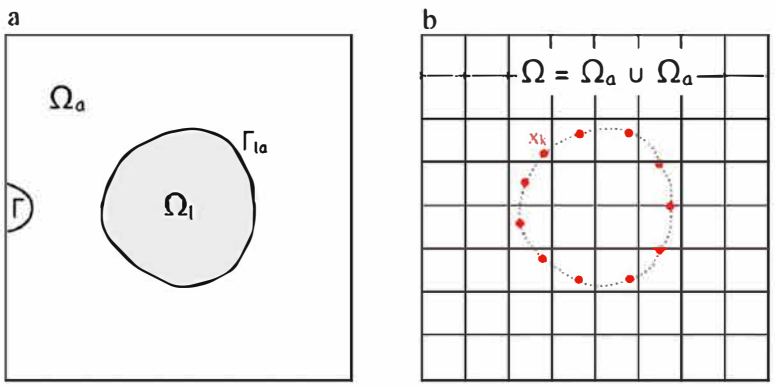

Figure 2. (a) Scheme of the continuous fluid problem with an "obstacle." (b) Scheme of the discrete fictitious domain problem.

In the absence of the obstacle Ω_I, the corresponding discrete finite element expression of the problem takes the form

$$\boldsymbol{KV}=\boldsymbol{F}_0 \tag{13}$$

where $\boldsymbol{V} \in \mathbb{R}^N$ is the vector of nodal unknowns, $\boldsymbol{F}_0 \in \mathbb{R}^N$ is the vector of nodal loads including the Dirichlet boundary condition on Γ, N is the number of nodes belonging to the mesh of Ω, and $\boldsymbol{K}$ is the $N \times N$ matrix of rigidity (we suppose $\boldsymbol{K}$ symmetric and invertible).

Now let $\boldsymbol{x}_k \in \mathbb{R}^2$ $(k \quad 1, \cdots, n_{Ia})$ be a given set of n_{Ia} points forming an independent mesh of the immersed boundary Γ_{Ia}. The finite element approximation of v at each point $\boldsymbol{x}_k$ reads

$$v(\boldsymbol{x}_k)=\sum_{i=1}^{N}\phi_i(\boldsymbol{x}_k)V_i=(\boldsymbol{\Phi V})_k \tag{14}$$

where ϕ_i is the interpolation function at node i, V_i is the ith component of $\boldsymbol{V}$, and Φ is the $n_{Ia}\times N$ matrix whose entries are the $\phi_i(\boldsymbol{x}_k)$ values. To ensure $v(\boldsymbol{x}_k)$ is close to $v_{Ia}(\boldsymbol{x}_k)$ (in a given sense), a source term is added on the right-hand side of (13)

$$\boldsymbol{KV}=\boldsymbol{F}_0+\boldsymbol{F}(q) \tag{15}$$

where q is an unknown source function defined on Γ_{Ia}.

Since any given v_{Ia} distribution may not be consistent with the problem (12) (for instance, in our case the linear problem (12) is the incompressible Stokes problem and v_{Ia} corresponds to the velocity of the solid boundary which, generally, does not conform with the incompressibility constraint), we proceed with a least squares method

$$\text{minimize} \quad J(q) : =\sum_{k=1}^{n_{Ia}}(v(\boldsymbol{x}_k) \quad v_{Ia}(\boldsymbol{x}_k))^2=||\boldsymbol{\Phi V} \quad \boldsymbol{v}_{Ia}||^2 \tag{16}$$

where $\boldsymbol{V}$ is given by (15) and $\boldsymbol{v}_{Ia} \quad (v_{Ia}(\boldsymbol{x}_1), \cdots, v_{Ia}(\boldsymbol{x}_{n_{Ia}}))$.

The last step consists of choosing the parametrization of the source function q. The simplest way is to define a ponctual distribution at the n_{Ia} control points $\boldsymbol{x}_k$: $q(\boldsymbol{x}) \quad \sum_k q_k\delta(\boldsymbol{x} \quad \boldsymbol{x}_k)$, where δ is the Dirac function. In this case, the assembled vector $\boldsymbol{F}(q)$ is simply given by

$$\boldsymbol{F}(q)=\boldsymbol{\Phi}^T\boldsymbol{q} \tag{17}$$

where $\boldsymbol{q}=(q_1, \cdots, q_{n_{Ia}})$.
Solving the least squares problem (16) for $\boldsymbol{q}$ gives the $n_{Ia}\times n_{Ia}$ linear system

$$\boldsymbol{kq}=\boldsymbol{v}_{Ia} \quad \boldsymbol{v}_0 \tag{18}$$

with $\boldsymbol{k} \quad \boldsymbol{\Phi K}^{-1}\boldsymbol{\Phi}^T$ and $\boldsymbol{v}_0 \quad \boldsymbol{\Phi K}^{-1}\boldsymbol{F}_0$ (which corresponds to the solution of the n_{Ia} control points in the absence of the obstacle).

We can make the following remarks:

1. When applied to the fluid-solid coupling problem, the physical field v is the fluid velocity vector and q corresponds to the distributed drag force acting on the immersed solid boundary Γ_{Ia}. Moreover, if the control points $\boldsymbol{x}_k$ form a subset of the solid mesh nodes, then the qk values determined by (18) are the corresponding nodal forces.

2. Other parametrizations for q are possible but lead to a slightly more complex implementation. If we choose for example q to take the form $q(\boldsymbol{x}) \quad \sum_k q_k \psi_k(\boldsymbol{x})$, where ψ_k are the interpolation functions on the mesh of Γ_{Ia}, then the resulting nodal source term has to be computed as $\boldsymbol{F}(q) \quad \boldsymbol{\Psi}^T \boldsymbol{q}$, where $\boldsymbol{\Psi}_{ki} \quad \int_{\Gamma_{Ia}} \phi_i(\boldsymbol{x}) \psi_k(\boldsymbol{x}) \mathrm{d}x$. Thus, intersections between the mesh of Γ_{Ia} and the mesh of Ω must be computed beforehand at each time. With this variant, our FDM is closely akin to the Lagrange multiplier fictitious domain of *Glowinski et al.* [1995].

3.2. Numerical Strategy for Implementing Solid-Fluid Coupling

Several approaches exist to tackle problems of fluid-structure interaction [*Felippa et al.*, 2001], ranging from the monolitic ones (in which the solid and fluid subproblems are solved simultaneously as they are formulated in a unique problem) to the staggered ones (in which the subproblems are solved separately and coupled at specific discrete time steps). The second approaches are more flexible since they allow the use of two separate codes and facilitate the use of nonmatching meshes. Our formulation belongs to this second kind and uses a semi-implicit time marching scheme for a stability purpose.

We recall that the solid domain Ω_I is discretized with a finite element mesh containing N_I nodes (with n_{Ia} nodes on its immersed boundary Γ_{Ia}), while the mesh of the fictitious fluid domain $\Omega \quad \Omega_o \cup \Omega_I$ is discretized with N nodes. At a given time t^{n+1}, the solid state is calculated according to (8), in which the force balance is modified to account for the fluid reaction $\boldsymbol{F}_{Ia}$ that acts on the n_{Ia} nodes of the immersed solid boundary Γ_{Ia}. In a purely explicit coupling procedure, this reaction is evaluated at the previous time step t^n, but unfortunately this easier scheme often turns out to be numerically unstable. The implicit variant improves stability but introduces the unknown reaction $\boldsymbol{F}_{Ia}^{n+1}$ at time t^{n+1}. A predictor-corrector-type algorithm is thus used, as follows. First, the solid nodal velocities vector can be expressed by

$$\dot{\boldsymbol{U}}^{n+1/2} = \dot{\boldsymbol{U}}_{free}^{n+1/2} + \Delta t \boldsymbol{M} \quad {}^{1}\boldsymbol{F}_{Ia}^{n+1} \tag{19}$$

where $\dot{\boldsymbol{U}}_{free}^{n+1/2}$ is the predicted nodal velocities vector in the absence of viscous fluid drag

$$\dot{\boldsymbol{U}}_{free}^{n+1/2} = \dot{\boldsymbol{U}}^{n \quad 1/2} + \Delta t \boldsymbol{M} \quad {}^{1}[\boldsymbol{F}_{int}^{n} + \boldsymbol{F}_{ext}^{n} \quad \boldsymbol{C}^{n}]. \tag{20}$$

Equation (19) can obviously be rewritten for the n_{Ia} nodes of Γ_{Ia}

$$\dot{\boldsymbol{u}}^{n+1/2} = \dot{\boldsymbol{u}}_{free}^{n+1/2} + \Delta t \boldsymbol{L} \boldsymbol{M} \quad {}^{1}\boldsymbol{F}_{Ia}^{n+1} \tag{21}$$

where $\dot{\boldsymbol{u}}^{n+1/2} \quad \boldsymbol{L}\dot{\boldsymbol{U}}^{n+1/2}$, $\dot{\boldsymbol{u}}_{free}^{n+1/2} \quad \boldsymbol{L}\dot{\boldsymbol{U}}_{free}^{n+1/2}$, and $\boldsymbol{L}$ is a $n_{Ia} \times N_I$ Boolean matrix (extraction matrix). The viscous fluid forces $\boldsymbol{F}_{Ia}^{n+1}$ acting on the solid mesh are given by

$$\boldsymbol{F}_{Ia}^{n+1} = \boldsymbol{L}^T (\quad \boldsymbol{a}^{n+1} \tag{22}$$

where $\boldsymbol{q}^{n+1}$ (the source terms) are, according to (18), solution of the linear system

$$\boldsymbol{k}^{n+1} \boldsymbol{a}^{n+1} = \dot{\boldsymbol{u}}^{n+1/2} \quad \boldsymbol{v}_i \tag{23}$$

where $\boldsymbol{k}^{n+1} \quad \boldsymbol{\Phi}^{n+1} \boldsymbol{K} \quad {}^{1}\boldsymbol{\Phi}^{n+1T}$. Let us recall that this system is "small" regarding to the whole grid size, since it involves only the control nodes of the solid's boundary.

Inserting (23) and (22) into (21), we obtain the corrected velocities by solving the linear system

$$(\boldsymbol{k}^{n+1} \boldsymbol{m} + \Delta t \boldsymbol{I}) \dot{\boldsymbol{u}}^{n+1/2} = \boldsymbol{k}^{n+1} \boldsymbol{m} \dot{\boldsymbol{u}}_{free}^{n+1/2} + \Delta t \boldsymbol{v}_i \tag{24}$$

where $\boldsymbol{m}$ is the nodal mass matrix of the n_{Ia} nodes (recall that $\boldsymbol{M}$ is diagonal).

Our coupling fluid-solid procedure can be summarized by the following flowchart:

1. Initialization: define the meshes of the initial solid domain Ω_i^0 and of the fictitious (fixed) domain Ω, define the initial solid state $(\boldsymbol{U}^0, \dot{\boldsymbol{U}}^0, \sigma^0)$ and the initial fluid state $(\boldsymbol{V}^0, \boldsymbol{q}^0 \quad 0)$.

2. Assemble and factorize the Stokes matrix $\boldsymbol{K}$ of the fictitious problem.

3. New time step: $t^{n+1} \quad t^n + \Delta t$.

4. Prediction stage: compute the predicted solid velocities $\dot{\boldsymbol{U}}_{free}^{n+1/2}$ from (20).

5. Extract the predicted velocities $\dot{\boldsymbol{u}}_{free}^{n+1/2}$ at the n_{la} solid boundary nodes of Γ_{la}.

6. Compute the matrix $\boldsymbol{k}^{n+1}$ and the source terms at the n_{la} control points from (23) using the predicted velocities $\dot{\boldsymbol{u}}_{free}^{n+1/2}$.

7. Compute the fluid velocities (if desired) by solving the Stokes problem

$$\boldsymbol{K}\boldsymbol{V}^{n+1} = \boldsymbol{F}_0 + \Phi^{n+1T}\boldsymbol{q}^{n+1}.$$

8. Correction stage: correct the velocities and positions of the n_{la} nodes by solving (24).

9. Update the stress σ^{n+1} of the solid and assemble the new internal and external forces $\boldsymbol{F}_{int}^{n+1}$, $\boldsymbol{F}_{ext}^{n+1}$, as well as the fluid-solid interaction by (22).

10. $n \leftarrow n+1$ and go to 3.

To resume, the main advantages of the FDM are:

1. To avoid repetitive remeshing in the fluid domain (calculations on a fixed mesh).

2. To handle complex geometries and still be able to use a Cartesian mesh, since the fluid domain has a simple shape.

3. The user can define which points on the solid boundary are coupled with the fluid. "One-way coupling" or "two-way coupling" is easy to handle. For instance in our applications, the top boundaries of solid plates are chosen to remain as free surfaces. This is an important advantage of our coupling method.

However, FDM also has the following disadvantages:

1. As we will see below, our variant of this method is only first-order accurate.

2. The fictitious domain method is only used for the fluid domain. Thus, the Lagrangian description used to resolve the evolution of solid plates still needs a remeshing technique for very large deformation.

3. For each control point in our coupling procedure, we need to compute the product of $\boldsymbol{K}^{-1}\Phi^T$, leading to a large number of linear systems to solve if their number is important.

4. Benchmarks and Examples

We shall now demonstrate the potential of our new coupling method with a few benchmarks and validations, in two dimensions. We emphasize that our FDM was also implemented in the finite element analysis program Dynaflow™ [*Prevost*, 1981], and some of the following examples were performed and compared with the two codes. We start with the benchmark of an analytical solution for a rigid solid immersed in a fluid (section 4.1) and then move on to problems considering a deformable solid, for which we compare our solution with other numerical solutions (sections 4.2 and 4.3). Then in section 4.4, we tackle the analog subduction experiment by *Guillaume et al.* [2009] which was also used as a benchmark in *Gibert et al.* [2012] and conclude in section 4.5 with a comparison with the community benchmark proposed by *Schmeling et al.* [2008].

4.1. An Analytical Stationary Solution: The Wannier Flow

As a first validation of our FDM in a 2D stationary case, we consider an analytical solution of Stokes flow problem called the Wannier flow [*Wannier*, 1950; *Ye et al.*, 1999]. It considers the viscous flow around a rigid cylinder rotating with an angular velocity ω near a wall in translation (see Figure 3a). The velocity and the pressure fields are resolved as

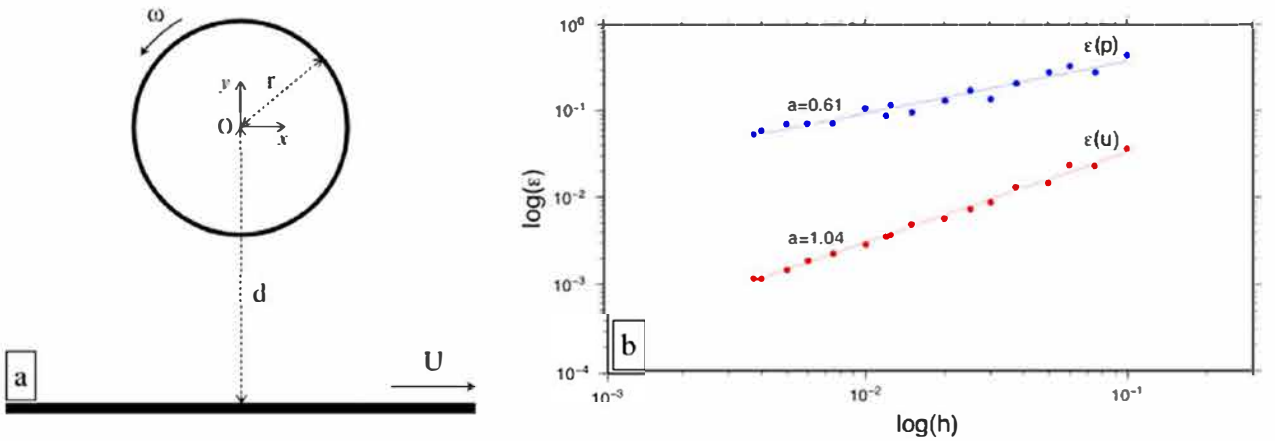

Figure 3. (a) Scheme of the Wannier flow [*Wannier*, 1950]. (b) L^2 discrete errors of velocity and pressure numerical field as a function of the mesh size h. The slope a of the lines represents the order of convergence for both the velocity and the pressure. The linear convergence is satisfactory regarding the Q1 elements used for the finite element discretization.

$$u_x = U \quad 2(A+F\tilde{y})\left[\frac{s+\tilde{y}}{\alpha}+\frac{s\quad\tilde{y}}{\beta}\right] \quad F\ln\frac{\alpha}{\beta}$$
$$B\left[\frac{s+2\tilde{y}}{\alpha}\quad\frac{2\tilde{y}(s+\tilde{y})^2}{\alpha^2}\right]$$
$$C\left[\frac{s\quad 2\tilde{y}}{\beta}+\frac{2\tilde{y}(s\quad\tilde{y})^2}{\beta^2}\right]$$
$$u_y = 2x\left[(A+F\tilde{y})\left(\frac{1}{\alpha}\quad\frac{1}{\beta}\right)\quad B\frac{\tilde{y}(s+\tilde{y})}{\alpha^2}\quad C\frac{\tilde{y}(s\quad\tilde{y})}{\beta^2}\right]$$
$$p = \quad \eta x\left[B\frac{s+\tilde{y}}{(\kappa+\tilde{y}s)^2}+C\frac{s\quad\tilde{y}}{(\kappa\quad\tilde{y}s)^2}+4F\frac{s\tilde{y}}{\kappa^2\quad\tilde{y}^2s^2}\right]$$

with

$$s=\sqrt{d^2\quad r^2},\quad \gamma=(d+s)/(d\quad s),\quad \tau=\omega r^2/2s,$$
$$A=\quad d(F+\tau),\quad B=2(d+s)(F+\tau),\quad C=2(d\quad s)(F+\tau),\quad F=U/\ln\gamma,$$
$$\tilde{y}=y+d,\quad \alpha=x^2+(s+\tilde{y})^2,\quad \beta=x^2+(s\quad\tilde{y})^2,\quad \kappa(x^2+\tilde{y}^2+s^2)/2$$

where x and y are the Cartesian coordinates in the plane, η is the viscosity of fluid, and other geometrical parameters can be viewed in Figure 3a.

The fluid domain is a square of edge length 1.5 m and is discretized by a regular mesh of size equal to h. We placed at distance intervals h_{cp} a certain amount of control points on the boundary of the cylinder which is placed at the center of the domain. We impose on the fluid domain boundaries the analytical solution that simulates an infinite medium and we impose the mean pressure to be equal to 0.

We produce a convergence diagram (Figure 3b) in which the analytical and numerical solutions for our fictitious domain method are compared, by computing the L^2 discrete error for each field. These results are close to those obtained with other nonmatching interface methods [e.g., *Ye et al.*, 1999].

We have performed a number of experiments with different mesh sizes varying the distance h_{cp} between control points, and we have identified an optimum distance that ranges between 1 and 2 times the grid mesh size. This range is also known in Lagrange multiplier fictitious domain methods [*Glowinski et al.*, 1995].

4.2. Sinking of a Competent Block Into a Viscous Medium

We consider here the coupling case of two deformable media found in *Gerya and Yuen* [2003], in which a competent block of density ρ_s 3300 kg .m ^{3} sinks into a viscous medium of density ρ_f 3200 kg .m ^{3} and of viscosity η_f 10^{21} Pa .s. The viscous medium is a square domain with edge lengths equal to 500 km, and its boundaries are set free-slip. The competent block is a smaller square with edge lengths equal to 100 km, initially placed at a distance of 50 km below the upper edge of the viscous domain.

The solid solver ADELI is used for the competent block, whereas another finite element direct solver is used to compute the Stokes flow for the surrounding fluid. The block is viscoelastic with a Young modulus equal to 10^{11} Pa , and three different viscosity values are tested (η_s 10^{22} Pa .s, 10^{23} Pa .s, and 10^{24} Pa .s). The Maxwell relaxation time is consequently less than 0.43 Myrs, and the elastic behavior of the block is thus negligible.

Results are displayed in Figure 4. The smaller the viscosity of the block, the more its deformation is important. The viscoelastic solid sinks faster at low viscosities because of the "aerodynamic" shape that it adopts. After 15 and 20 Myr, the height and shape of the block are similar to those displayed by *Gerya and Yuen* [2003] for different viscosities.

4.3. Bending of an Elastic Plate

We perform the numerical experiment proposed by *Bonnardot et al.* [2008a] in order to compare their results obtained with a remeshing coupling technique, with our results obtained with the fictitious domain method.

This two-dimensional numerical experiment consists of an elastic plate of length l 3 m and thickness e 0.2 m immersed in a fluid channel of width L 6 m. A fluid of viscosity η 10^5 Pa s is injected in the channel with a prescribed horizontal velocity v 60 m/s. The duration of the experiment is T 1 s. The plate bends until it reaches equilibrium. Figure 5a displays the final pressure and velocity vectors in the fluid.

In *Bonnardot et al.* [2008a], both the solid and the fluid domains were discretized with unstructured meshes that match exactly at their interface. Periodic remeshing of the fluid domain was needed during the evolution due to the solid motion. The solid's boundary velocity was imposed as a Dirichlet condition to the fluid mesh.

We display in Figure 5a the pressure field when the static solution is reached. The bent plate is represented in gray and some of its intermediate positions are drawn in dashed gray line. For comparison, we show in Figure 5b the evolution of the displacements of the bottom-left corner of the plate obtained with our coupling using the fictitious method (solid line) and those obtained with a remeshing technique. Results are similar.

4.4. A Laboratory Test of Subduction by Guillaume et al. [2009]

Numerous analog models have been developed in order to understand different aspects of subduction dynamics. We can class laboratory subduction studies into three classes. The first class considers freely subducting plate dynamics [*Schellart*, 2004; *Bellahsen et al.*, 2005], i.e., the system is only driven by the slab-pull force. In the second class, a kinematic condition is imposed to the far edge of the subducted plate [*Funiciello et al.*, 2004], but the upper plate is absent. A third class of laboratory experiments includes the application of a plate velocity and also takes into account the upper plate [*Heuret et al.*, 2007; *Espurt et al.*, 2008; *Guillaume et al.*, 2009]. This last category is the one that we consider with our numerical approach.

In this section, we aim at reproducing, at the laboratory scale, the reference model of *Guillaume et al.* [2009], as did *Gibert et al.* [2012]. Although in *Gibert et al.* [2012] the numerical results were close to those obtained in the laboratory experiment, minor differences had been attributed to the absence of a viscous mantle. With the coupling method presented here, we are able to test the effect of an underlying viscous material.

In the laboratory experiment, a viscoelastic silicone material was taken to simulate tectonic plates. These plates were placed above glucose syrup (mantle) inside a Plexiglas tank. A rigid piston pushed the subducted plate on the far edge, while the upper plate was held fixed. The bottom of the tank represented the 660 km depth boundary. Parameters are summarized in Table 1. Note that the coefficient of friction

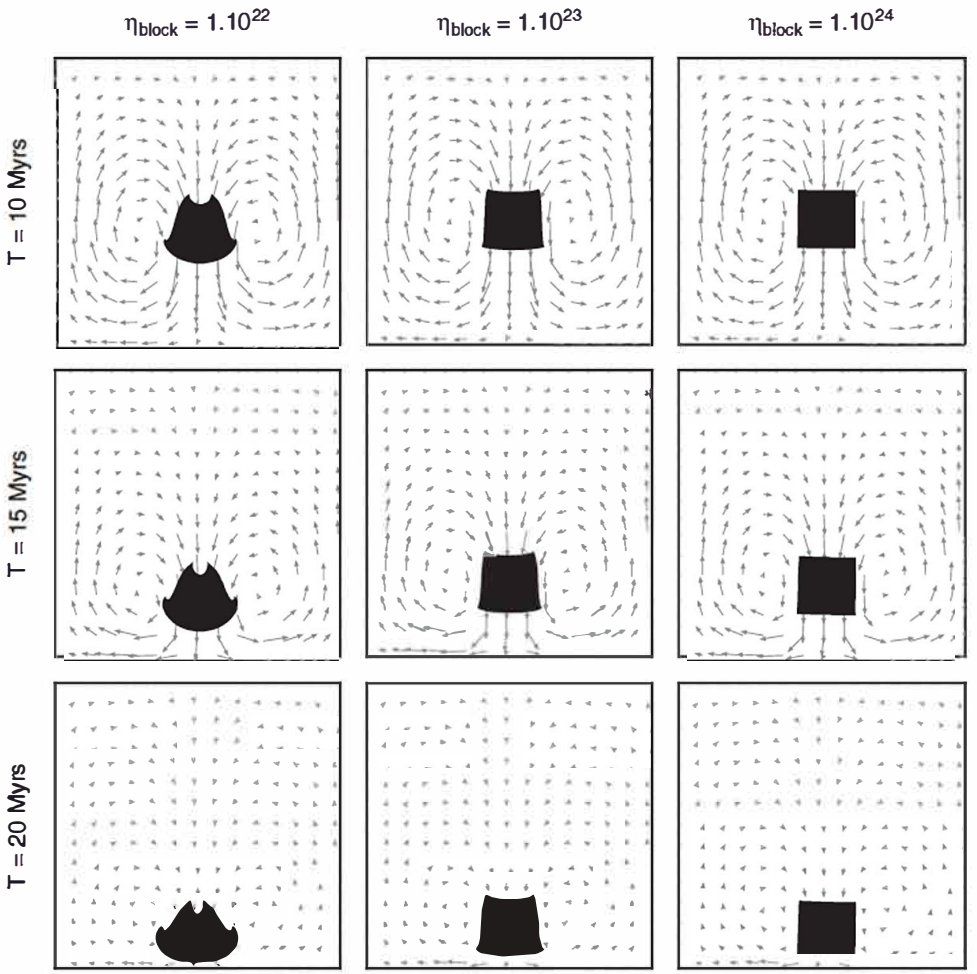

Figure 4. Sinking block benchmark [from *Gerya and Yuen*, 2003]. Results for three viscosity ratios η_s/η_f: 10, 100, and 1000.

between the plates and between silicone and plexiglass are difficult to quantify precisely in analog models, whereas one must always provide them in the numerical models.

The Dirichlet conditions on the boundary of the fluid domain in the numerical experiment are chosen as follows: normal and tangential velocities at the bottom and edges boundaries are equal to zero. Because there can be vertical motion of the solid, we cannot assume a free-slip top boundary of the fluid domain at the same depth level as for the solid (problem of consistency of the control points' velocities and this boundary condition). Thus, we immerse the solid well below the top boundary of the fluid, in order to safely set the fluid top boundary as free-slip. Consequently the fluid domain is divided into two. The first main domain defines the area located in between the bottom of the tank and depth 5 mm and has the viscosity of the glycose syrup. The second domain extending from depth 5 mm to +3 mm (the plates' domain is initially set between 0 and depth 13 mm) has a weaker viscosity of 10 ^{6} Pa .s and a density equal to 0. Note that we do not account for the viscous drag exerted on the upper boundary points of the solid plates, so that the latter remain free-surfaces ("one-way coupling").

Figure 6 displays the comparison between the numerical results and the laboratory test by *Guillaume et al.* [2009]. The first column shows the results obtained with an inviscid fluid (no coupling with the fluid solver, similarly to *Gibert et al.* [2012]). The second column displays the result accounting for a fluid of viscosity 82 Pa s equal to that of the glucose syrup used in the laboratory experiment by *Guillaume et al.* [2009] (third column). Despite the need to assume an arbitrary friction coefficient in the mechanical models, the numerical result confirms that the viscous fluid in this experiment has a negligible effect on the slab evolution.

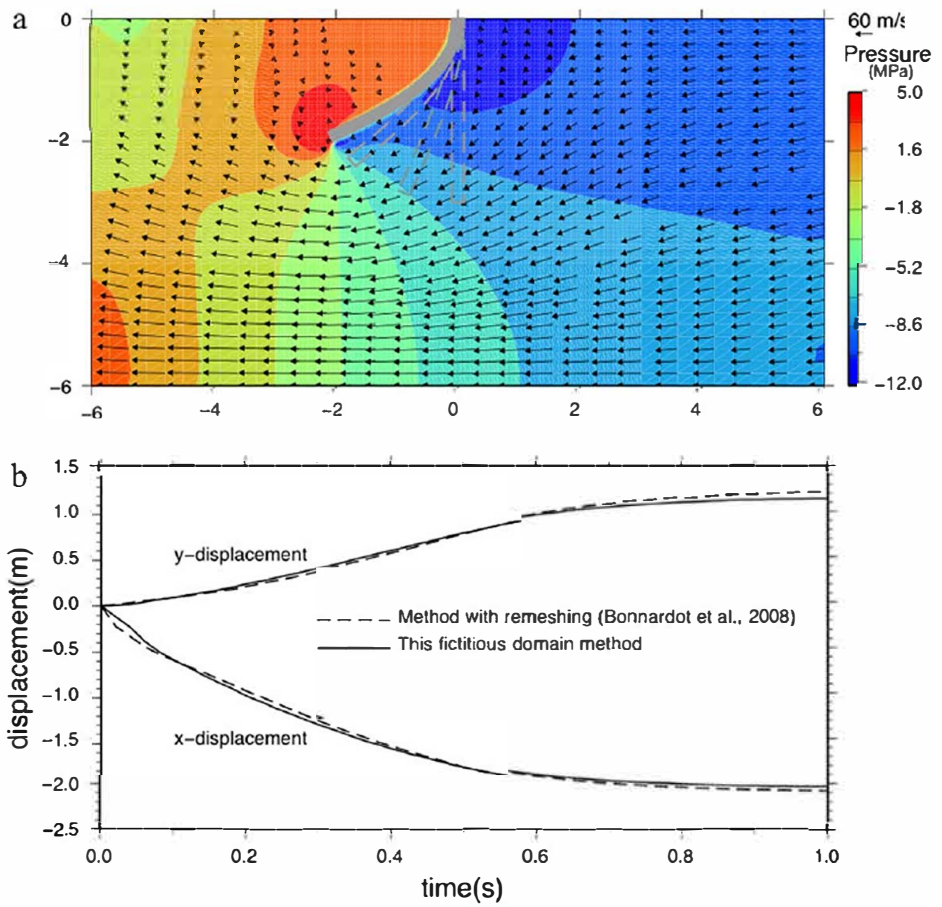

Figure 5. (a) Pressure and velocity fields for the experiment of an elastic plate bent by a viscous flow. (b) Displacement of the bottom left corner of the plate over time.

Figure 6d displays the result obtained with a greater value of the analog mantle viscosity, equal to 500 Pa s, which corresponds to a mantle viscosity of 10^{21} Pa .s at the natural scale. With this viscosity, the modeled subducted plate does not fold but rather bends smoothly backward. The viscous drag along the plate is stronger. Consequently, penetration of the subducted plate is harder and the far-field kinematic boundary condition is accommodated by greater internal deformation than in the analog model. Moreover, the experiment produces a huge arc bulge, unrealistic at the natural scale. Actually, this bulge results from our choice of an arbitrarily high plate interface friction coefficient μ 0.4, which allows to match the internal deformation of the numerical and the analog models. This value is obviously unrealistic for a subduction interface, and in the following models, we have chosen friction values less than 0.1, consistent with those reported in the literature [*Cattin et al.*, 1997; *Lamb*, 2006].

This experiment with an extreme mantle viscosity of 500 Pa s shows the drastic effect of the underlying mantle viscosity on the subducting plate geometry. The shape of folds is modified and at least, delayed in time. Overriding plate deformation (shortening or extension) is also affected. We will mainly focus on these points in section 5 when studying real scale subduction zones.

4.5. Community Benchmark by Schmeling et al. [2008]

We perform the benchmark test proposed in *Schmeling et al.* [2008]. It allows to compare our results with those obtained with several others types of codes (finite differences or finite elements, Lagrangian or Eulerian). This 2D benchmark consists in the sinking of a competent and dense body (simplified L-shaped plate with a horizontal length of 2000 km) driven only by internal forces into a viscous mantle down to 700 km depth.

Table 1. Mechanical Parameters for the Test Described in Section 4.4[a]

Parameters	Values Used in the Reference Model	Equivalence at the Natural Scale
Plate thickness, e	13 mm	90 km
Density contrast, $\Delta\rho = \rho_l \quad \rho_m$	76 kg.m^{-3}	76 kg.m^{-3}
Plates viscosity η_l		
Subducting plate	5.0×10^5 Pa.	1.3×10^{24} Pa.s
Overriding plate	3.0×10^5 Pa.s	7.7×10^{23} Pa.s
Young modulus, E	5000 Pa*	4.9×10^{10} Pa
Poisson ratio, ν	0.25*	0.25
Friction coefficient, μ		
Plates interface	0.4*	0.4
Plate/660 km discontinuity	0.02*	0.02
Fluid viscosity, η_a	82 Pa s	1.64×10^{20} Pa.s

[a]The set of parameters marked with * are not evaluated in *Guillaume et al.* [2009] and have been arbitrarily chosen in order to reproduce as best as possible the laboratory results.

We consider a viscoelastic material for the modeled slab. We assume a Young modulus of 184 GPa and a Poisson ratio of 0.244 corresponding to the values used in the Lapex-2D code (details in *Schmeling et al.* [2008]). The relaxation time (about 40 Kyr) is very small in comparison to the time of the experiment, and thus the effect of slab elasticity is negligible.

The top surface of the plate is free-surface and its right-edge is fixed. The other edges of the plate are coupled with the fluid. To avoid big mesh distortions in the solid, its remeshing is prescribed every 10 Myr. For the fluid domain, the bottom and edges are set free-slip, but for the top boundary we explore four types of conditions (see scheme Figure 7). Type 1 is top-open. In type 2, the top boundary is free-slip. In the other two types we add a zero-density layer with a viscosity equal to that of the mantle (type 3) or equal to 10^{19}Pa .s (type 4).

In Figure 8 our results are compared with those obtained with codes assuming a free-surface in *Schmeling et al.* [2008] (solid lines). The vertical position of the slab tip in time is similar for all four types of boundary conditions tested for the fluid domain (dashed lines). They follow the same slope as experiments using codes LAPEX 2D and LaMEM (coarse meshes) until 45 Myr. These results are obtained, in our case, with the upper-left corner of the slab never sinking into the mantle (similar in its effect to the "numerical-locking" of the wedge described by *Schmeling et al.* [2008]).

We perform an additional experiment in which we couple the points at the plate's top-surface with the fluid, so that the plate can sink below a threshold depth (Figure 8, purple line with circles). Then, the slope of the sinking slab, from about 30 Myr onward, becomes similar to that obtained without "numerical locking" at the wedge and with the viscous code FEMS-2D. However, the change in slope always remains more abrupt with our solution. Nevertheless, one must realize that when modeling a realistic subduction zone, this problem is not relevant since an overriding plate is present.

In Figure 8, we note negligible differences in cases with (types 3 and 4) and without (types 1 and 2) the additional zero-density low-viscosity layer. The flow in this layer has no effect on the bulk flow of the mantle, and thus on the evolution of the solid domain. Consequently, in our subduction models, we shall incorporate this layer only to consistently deal with both the free-slip boundary condition on the fluid and the free top surface condition on plates (also considered when benchmarking the laboratory experiment).

5. Effects of Mantle Viscosity on Subduction Cyclicity

Evidences for episodic development of the Andean orogeny have been noted for decades. *Steinmann et al.* [1929] and *Mégard* [1984] reported episodes of continental shortening separated by periods of relative quiescence. Recently, *Folguera and Ramos* [2011] identified three flat slab domains since Cretaceous times in the Southern Andes. In the Central Andes, a compilation of isotopic and geochronological data by *Haschke et al.* [2006] showed that arc magmatism migrated every 30–40 Myr since about 100 Myr, leading the authors to propose a link with cyclic episodes of flat subduction (the latter marking magmatic gaps). *Martinod et al.* [2010] also proposed a link between compressional events during the Cenozoic, with periods of increasing plate convergence and flat subduction in specific areas along the margin.

Haschke et al. [2006] related episodes of horizontal subduction with possibly repeated slab break-offs. Horizontal subduction is also commonly associated to the resisting subduction of a buoyant oceanic plateau. However, the validation of this mechanism remains problematic along the Andean margin (see discussion

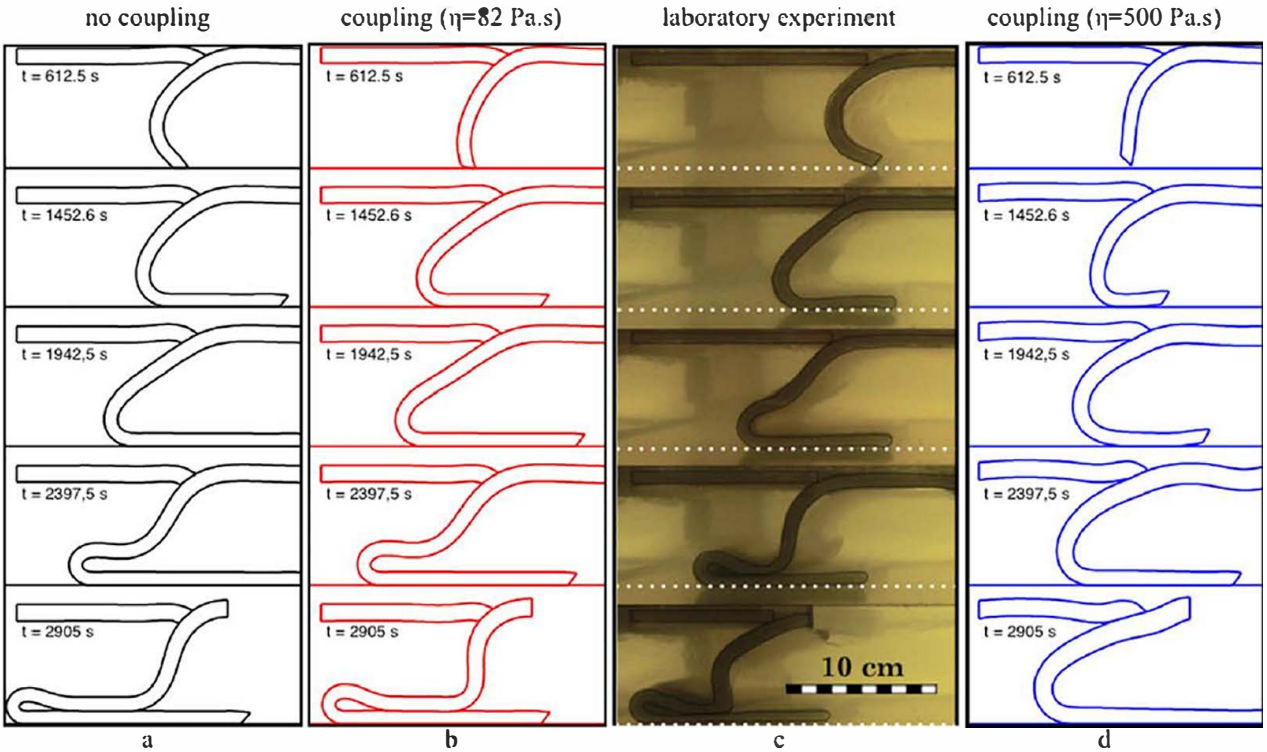

Figure 6. Comparison between (a, b, d) numerical models and (c) the laboratory result of *Guillaume et al.* [2009] for different values of the mantle viscosity.

in *Gibert et al.* [2012] and *Gerbault et al.* [2009]) and with statistics on subducting ridges carried out worldwide [*Skinner and Clayton*, 2013].

Here similarly to the previous numerical study by *Gibert et al.* [2012], we explore another cause for slab dip evolution. Indeed, depending on far-field plate kinematics, the development of slab folding, as it deposits on the 660 km depth boundary, may periodically flatten the slab. If v_{sp} and v_{op} refer, respectively, to the subducting and overriding plate velocities, counted positive toward the trench, cyclic folding was found to occur when $|v_{op}| < v_{op}+v_{sp}$ [*Gibert et al.*, 2012]. These cycles span about 20 Ma, less than the 30–40 Myr cycles reported for the Andes. Here we aim at testing the effect of mantle viscosity on subduction geometry and periodicity.

5.1. Model Assumptions

Our physical model described in section 2 (and similar to that of *Gibert et al.* [2012]) is valid under both conditions that thermal effects are negligible and that rheology is time independent. Dynamics of subduction

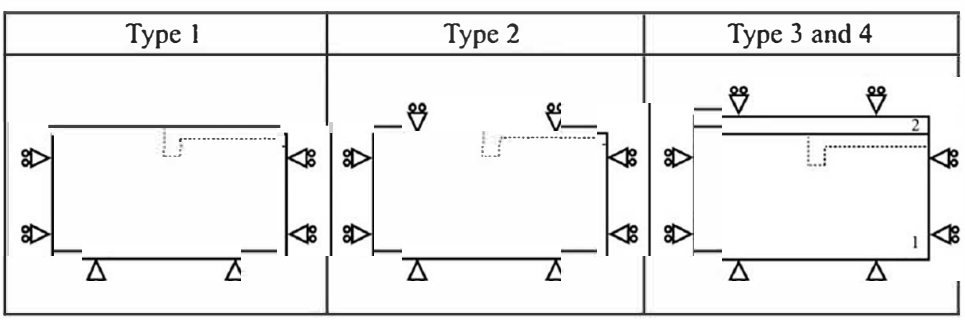

Figure 7. Free surface benchmark in *Schmeling et al.* [2008]. Four different boundary conditions on our fluid domain are tested, whereas the solid plate (represented by the dashed line) remains a free surface.

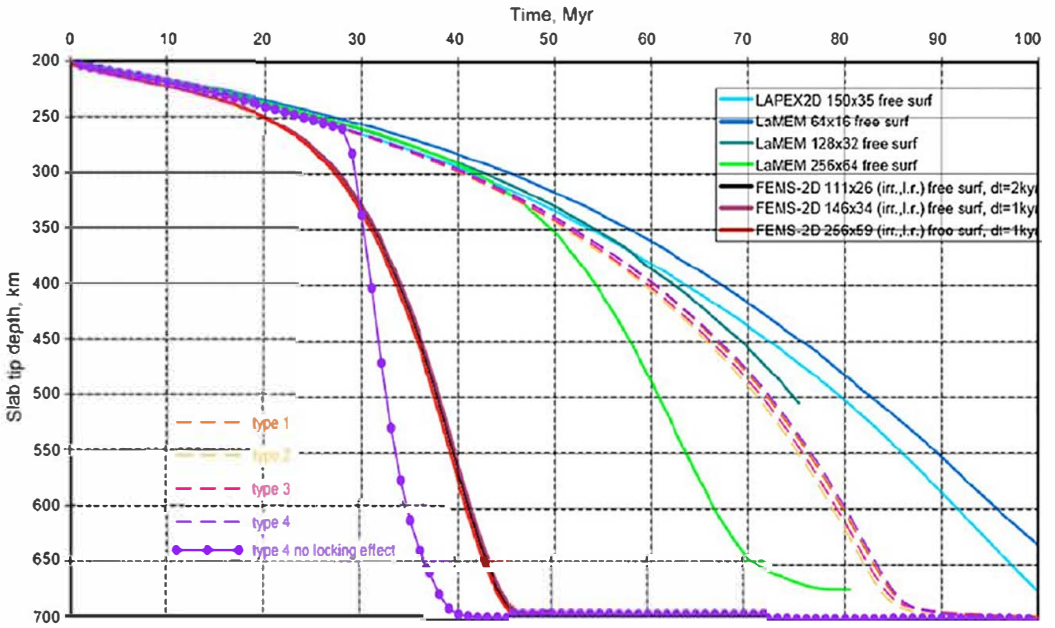

Figure 8. Position of the slab tip in time, modified after Figure 10 in *Schmeling et al.* [2008] for free surface codes. Our results are represented with dashed lines and with purple lines with circles. The colors represent different boundary conditions tested for the top of the fluid domain with our code and detailed in Figure 7. All of our results are obtained with the same meshes for both the fluid and the solid domains (h_{fluid} =10km and h_{solid} =15km).

can remain uncoupled from thermal effects if advection dominates overdiffusion, which is described by the Péclet number

$$Pe = \frac{H_{um} v_s}{\alpha} \tag{25}$$

where H_{um} 660km is the system's characteristic length, v_s its velocity, and α the thermal diffusivity. Taking for the Andes $v_s \simeq$ 7cm .yr ^{1}, the subduction velocity, and $\alpha \simeq$ 8.6.10 $^{7} m^2 .s^{1}$ according to *Sobolev and Babeyko* [2005], we obtain $Pe > 10^3 \gg 1$, which justifies that we neglect thermal effects in our dynamic model.

We define the model setup described in Figure 1 with terrestrial scale mechanical parameters given in Table 2. The fluid is a rectangular domain of size 9000 km $\times$ 685 km. We impose the following Dirichlet conditions: the bottom of this fluid tank is closed and its velocities are set to zero. The lateral edges are open, and the top is set free-slip. As described above, we separate this domain in two subdomains, first one between depth 660 km and 35 km corresponding to the viscous mantle, and another one between 35 km and 25 km with a very low viscosity (10^{10}Pa .s) and a density equal to 0. The top surfaces of both solid plates are still free-surfaces.

The far-field kinematic boundary conditions are set so that the velocity of the overriding plate is v_{op} 4.3cm .yr ^{1} and that of the subducted plate is v_{sp} 2.9cm .yr ^{1} (i.e., v_s 7.2cm .yr ^{1} according to evaluations for the South American and Nazca plates [*Somoza and Ghidella*, 2005]). The total time of the experiment is 127 Myr.

5.2. Results

We define a reference experiment with a mantle viscosity of 10^{20}Pa .s. The resulting evolution in time is shown in Figure 9, which displays plates geometry and deviatoric stress $J_2(\sigma'_p)$, together with the velocity and dynamic pressure fields within the mantle.

Folds form successively through time. During this periodic folding, note that the dip of the subducting plate varies at shallow-depth depending on the stage of fold development. As a fold forms, the slab dip

Table 2. Mechanical Parameters for the Subduction Model in Section 5

Parameters	Values
Plates thickness, e	90 km
Plates density, ρ_l	3200 kg.m^{-3}
Plates viscosity η_l	10^{24} Pa s
Young modulus, E	10^{11} Pa
Poisson ratio, ν	0.25
Friction coefficient, μ	
Plate interface	0.015
Plate/660 km discontinuity	0.2
Mantle density, ρ_a	3150 kg.m^{-3}
Mantle viscosity, η_a	0 10^{21} Pa s
Gravity, g	9.81 m.s^{-2}

decreases and moves close to the base of the overriding plate. When the fold ends, the dip of the slab increases back to a maximum of nearly 60°.

The velocity field in the fluid also changes during fold development. The upper image shows a relatively unidirectional velocity field that follows the direction of the slab rollback. Then, with the beginning of fold formation, the velocity field ahead of the subducted plate moves forward (leftward). Below this subducting plate, there is a "circulation zone," but the magnitude of velocities remains low. The last figure represents the stage at which the recently formed fold entrains the fluid down with its deposition. In this last stage, the magnitude of velocities regains that of subduction (or the reference velocity). This fourth image is similar to the first stage (slab rollback). Note that during fold development, in the mantle, a large zone of relatively high dynamic pressure develops in between the overriding plate and the flattening slab. Yet with the present mantle viscosity, pressure never exceeds 10 MPa. On the other hand, within a plate, high deviatoric stresses (>1 GPa) occur in its most bent parts. Values greater than 2 GPa are achieved from about 400 to 660 km depth within the bottom fold on the transition zone. These high values of $J_2(\sigma'_p)$ within the plate are not induced by the mantle flow nor drag but by its own folding.

The next numerical experiments aim at studying the effect of varying mantle viscosity with respect to the reference experiment above as well as with an experiment with an inviscid mantle. Figure 10 displays five cases with different mantle viscosities after 126.8 Myr of subduction. We represent the final geometries of plates, and their intermediate geometries are displayed with black lines for different times. Two independent color scales are used to describe the second invariant of the deviatoric stresses in the plates $J_2(\sigma'_p)$ and in the mantle $J_2(\sigma'_m)$.

Figure 10 (top) displays the result without a viscous mantle (as in *Gibert et al.* [2012]). Experiments with mantle viscosities lower than 10^{20} Pa s do not show any effect on the period nor on the size of slab folds. A shift in time (and space) of the formation of the first fold is detected at best. Mantle viscosity needs to be greater than 10^{20} Pa .s in order to generate an increase in the folding period (Figure 10b). For mantle viscosities up to 5.0×10^{20} Pa .s (Figures 10c and 10d), the folds' width and height both increase with increasing viscosity, because the viscous fluid under the fold prevents the plate from falling and folding. As a consequence, the time spent in folding is longer. Comparing Figure 10a with Figure 10d, we note that during folding, the amplitude of the curved part of the subducted plate is greater, thus the resulting fold is bigger.

Both cases in Figures 10a and 10d display a stage at which the subducting plate adopts a horizontal increasing shape in between 100 and 200 km depth. Actually, this behavior occurs for all viscosities lower than 5.0×10^{20} Pa .s.

For greater viscosities (8.0×10^{20} Pa .s and 10^{21} Pa .s, Figures 10e and 10f), we denote a change in the regime of fold formation. Fluid escape under the subducting plate becomes difficult. Thus, fold deposition is slower and bumps form. These "bumps" rise to nearly 250 km of depth, which seems unrealistic (no tomography has reported such a geometry). Furthermore, the slab cannot flatten in the upper 200 km depth, because material between the overriding plate and the top of the subducting plate is too viscous.

The $J_2(\sigma'_p)$ stress field in the mantle increases in magnitude with increasing mantle viscosity. While, for a mantle viscosity of 10^{20} Pa .s, the deviatoric stress never exceeds 10 MPa (cf., Figure 9), for a larger viscosity of 10^{21} Pa .s it is at least twice (Figure 10f).

On the other hand, maximum values of $J_2(\sigma'_p)$ in plates are not proportional to an increase in mantle viscosity. For low mantle viscosities, more than 2 GPa are achieved within the fold hinges below 400 km depth (Figures 10b–10d). In contrast for high mantle viscosities ($\geq 8.0\times10^{20}$ Pa .s), slab deposition occurs with little curvature, e.g., the plate is less bent and consequently $J_2(\sigma'_p)$ rarely exceeds 1 GPa.

Other numerical studies that account for a self-consistent temperature-dependent viscosity consider a lower or similar maximum slab strength (1 GPa) [e.g., *Čížková et al.*, 2002; *Billen*, 2010], which sets a lower

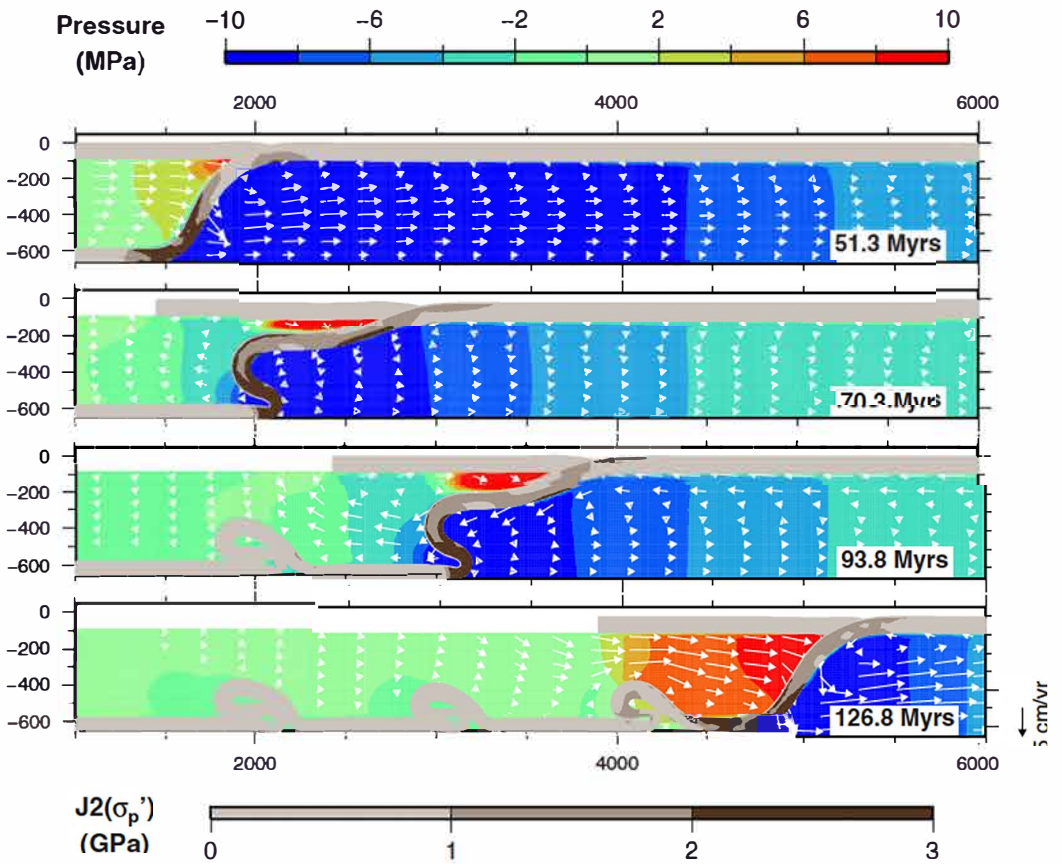

Figure 9. Reference model with a mantle viscosity of 10^{20}Pa .s. Geometry of plates, second invariant of the deviatoric stresses in the plates, dynamic pressure and velocity fields in the mantle at different stages.

limit to the upholding of the slab's coherency. Laboratory experiments on olivine samples produce similar values for temperatures around 1000°C and high pressure [*Weidner et al.*, 2001], while others obtained plastic yielding above 2.5 GPa [*Schubnel et al.*, 2013]. Our modeled slabs exceed 2 GPa rather locally in the sharp bends of folds at 400–660 km depth, which gives us confidence that the slab's mechanical coherency is preserved (even though brittle failure and nonlinear flow mechanisms obviously occur during slab folding). And if the slab does "break" completely, the remnant upper part of the slab will still pile up over its previously deposited slice, leading to a similar geometry at the large scale. A future step of our study is obviously to account for more complex and self-consistent rheology.

5.3. Effect on Slab Dip and Overriding Plate Stress Regime

Figure 11a shows temporal variations in the slab dip angle averaged between depths of 100 and 160 km. The "folding period," corresponding to the time-span between two lowest slab dips, is close to 20 Myr for $\eta_a \leq 10^{20}$Pa .s and reaches 30 and 40 Myr if η_a $3.0\times10^{20}$and 5.0×10^{20}Pa .s, respectively. Slab dip amplitudes span a range from about 5° to 45°, oscillating less with increasing mantle viscosity. The minimum dip attained by the slab also reduces with increasing mantle viscosity. This minimum value actually corresponds to a very flat slab extending over a length of nearly 500 km at about 150 km depth (see the geometry evolution of the top of the subducted plates in Figure 10). Note also that this depth may be reduced if one uses thinner viscoelastic plates (here we assumed 90 km; Table 2). These numbers compare with observations of the present-day flat slab in Central Chile, extending for about 350 km eastward at about 110 km depth [*Marot et al.*, 2013].

Figure 11b shows that the far-field horizontal stress of the overriding plate changes also depending on mantle viscosity. Positive values correspond to a tensile regime while negative values correspond to a

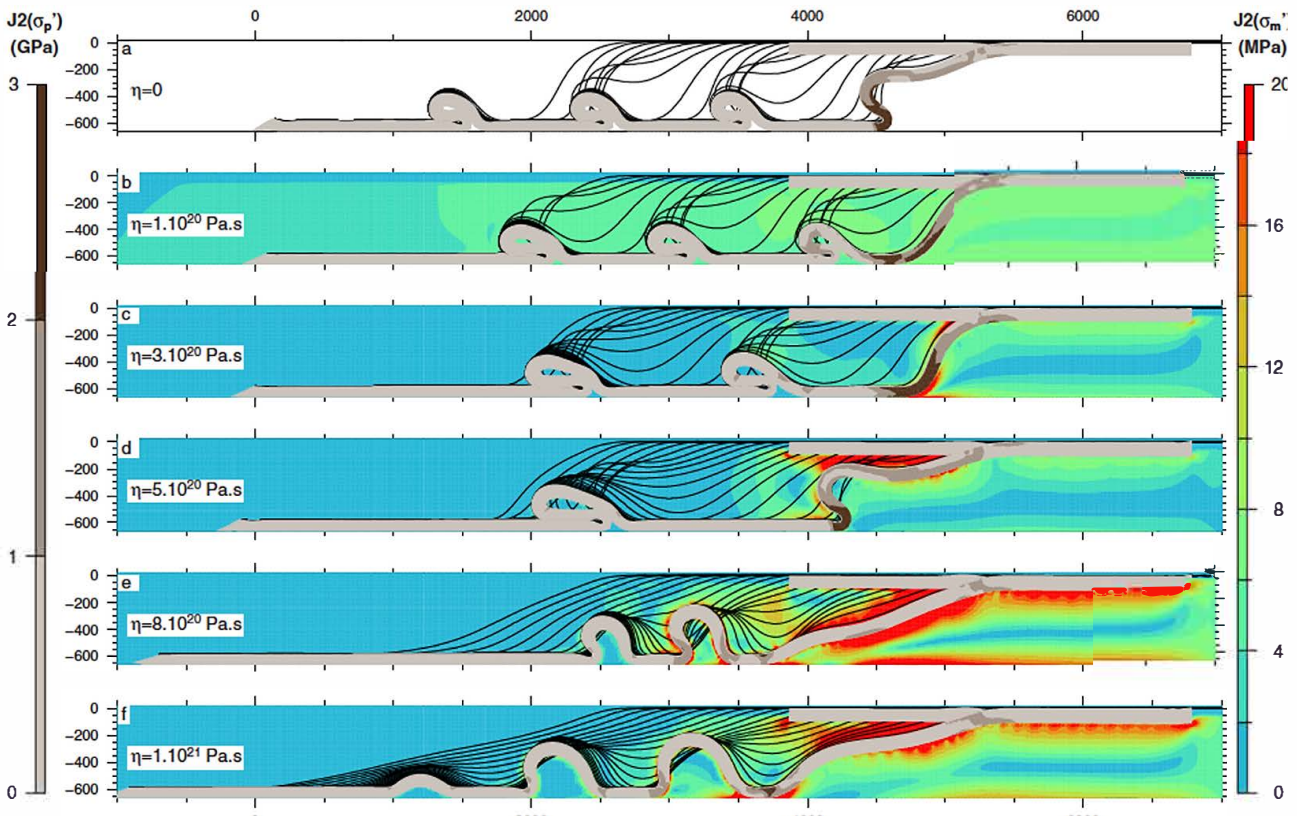

Figure 10. Geometries and second invariant of the deviatoric stresses (after 126.8 Myr) for models with different mantle viscosities. Two color scales are used for the stresses in the plates (gray scale to the left) and for those in the viscous mantle (blue to red scale to the right). The black lines show the shape of the top surface of the subducted plate at different times.

compressional regime. With a mantle viscosity of 10^{20} Pa .s, tensile and compressional periods alternate, similar to the inviscid case shown by *Gibert et al.* [2012]. With mantle viscosities equal to 3.0×10^{20} Pa .s and higher, the state of stress remains always compressional. Yet variations of about 100 MPa occur in all cases, which should still produce significant variations in tectonic structures.

Comparing the temporal evolution of the horizontal stress and the slab dip in Figure 11, we note that the slab dip that corresponds to the transition between compressional and tensile regimes is located around 40°. This value is in agreement with the conclusions drawn from the statistical study by *Lallemand et al.* [2005].

5.4. A Mantle With Two Viscosity-Layers

Rheological studies showed that the viscosity in the mantle varies with depth due to mineralogical phase transformations (olivine, spinel, wadsleyite, ringwoodite [e.g., *Karato and Wu*, 1993]) including the 660 km depth transition zone which constitutes a major jump in viscosity and density. However, it is not clear whether this jump is sharp or progressive, and it seems to vary worldwide. The results described above were obtained with an isoviscous upper mantle. We now perform numerical experiments in which the upper mantle is divided into two layers above and below 200 km depth, according to the approximate limit of low seismic shear waves (also called the Lehmann discontinuity zone).

Results are displayed in Figures 12. The weak upper mantle layer is assigned a viscosity of 1.0×10^{20} Pa .s in the cases of Figures 12a and 12b. The more viscous layer underneath is assigned a viscosity equal to 5.0×10^{20} Pa .s (Figure 12a) and 1.0×10^{21} Pa .s (Figure 12b). A third case is presented in Figure 12c, in which the viscosity of the weak layer is set to 1.0×10^{19} Pa .s whereas the layer below has a viscosity of 1.0×10^{21} Pa .s.

Figures 12b and 10d show a strong similarity, indicating that the viscosity directly under the overriding plate plays a first-order role in the formation of folds. Whereas in the isoviscous case, the fluid between the

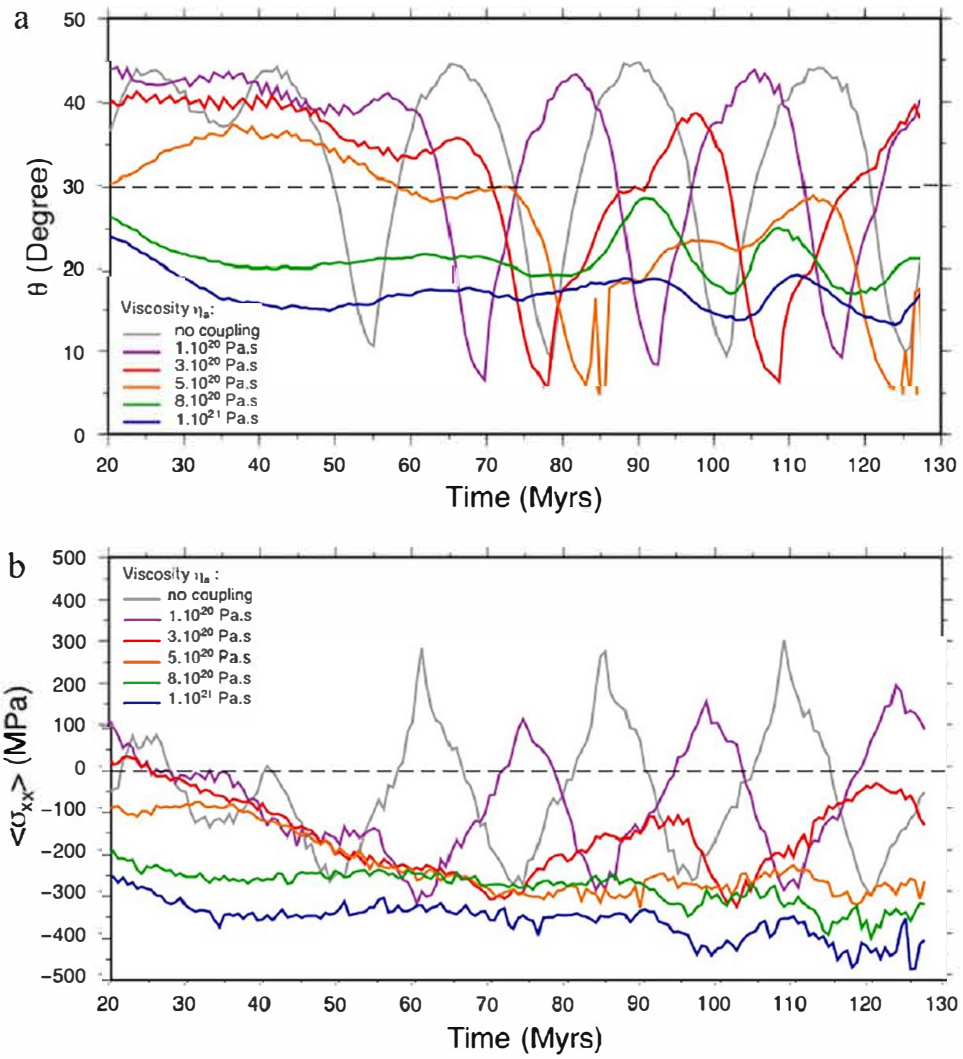

Figure 11. (a) Temporal evolution of the slab mean dip angle taken between 100 and 160 km of depth for different mantle viscosities. (b) Temporal evolution of the overriding plate state of horizontal stress, for different mantle viscosities.

slab and the overriding plate is evacuated with difficulty; here, the weak upper mantle layer allows plate rising during folding. Nevertheless, we see that the folds are bigger when η 10^{21}Pa .s (cases of Figures 12b and 12c), a behavior that is linked with the facility of the fluid to evacuate under the folded subducting plate.

These bilayered models indicate that the folding length periods are controlled by the average viscosity of the mantle. Let us evaluate both the arithmetic and the geometric weighted means (respectively, η_{ari} and η_{geo}) of the viscosity, in which the weight corresponds to the layers' thicknesses under the lithosphere. We obtain η_{ari} 6.99×10^{20}Pa .s and η_{geo} 4.64×10^{20}Pa .s. Comparing qualitatively Figure 10 and Figure 12c for an isoviscous mantle model, we observe that the bilayered case is an intermediate case between a uniform viscosity of 3.0×10^{20}Pa .s (Figure 10c) and 5.0×10^{20}Pa .s (Figure 10d). Therefore, a constant mantle viscosity corresponding to the geometric mean appears to be an appropriate approximation of the mantle's behavior (without questioning the necessity to consider realistic properties).

6. General Discussion and Geodynamic Application

6.1. A Brief Review of Slab Folding Studies: Comparison With our Results

Previous "free-subduction" studies have focused on slab deposition modes on the upper-lower mantle discontinuity, such as *Schellart* [2008] and *Ribe* [2010]. First, note that the slab's behavior was explored at the

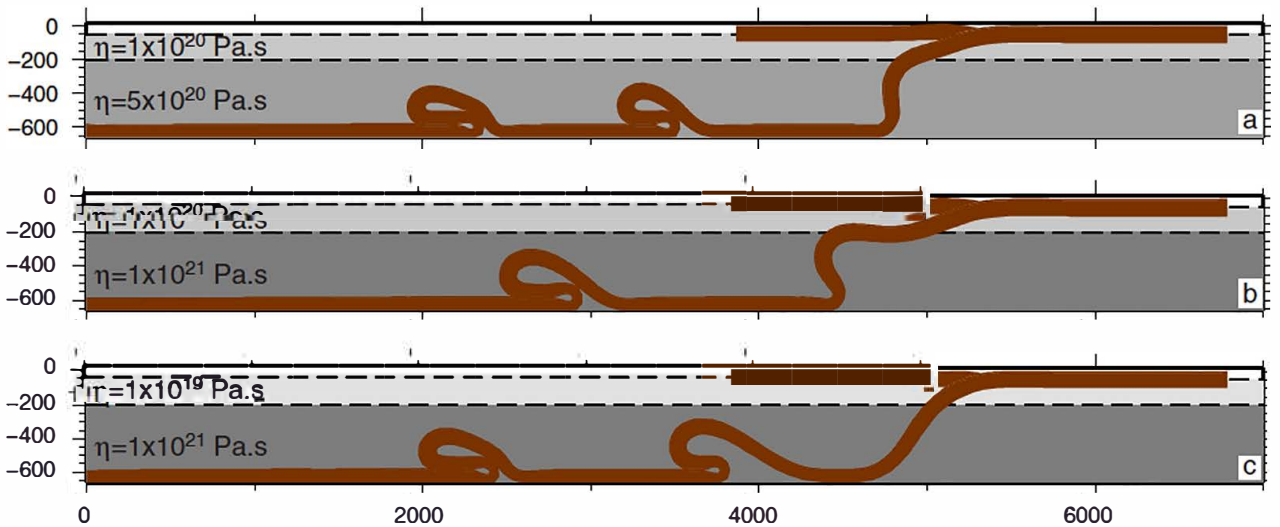

Figure 12. Final configurations for a double layer mantle.

onset of deposition, whereas we study conditions for folding cyclicity on the ≥100 Myr time scale. With analog models of free-subduction, *Schellart* [2008] determined four deposition modes depending on the values of the mantle-plate thickness ratio β H_{um}/e and the slab-mantle viscosity ratio γ η_p/η_a. These modes were linked with a range of values of the slab's radius of curvature prior to deposition. Later on, with a numerical approach, *Ribe* [2010] also related deposition modes and slab dip just before it reaches the discontinuity, as a function of β and γ. These two studies provide consistent results, with a small slab dip correlating with a large radius of curvature. Our modeled plate and mantle thicknesses lead β 7.3, placing us in the Strong Retreating (SR) mode (see the diagram of *Schellart* [2008]), whatever the value of γ. However, according to the diagram of *Ribe* [2010], there should be a transition from the Folding Retreating (FR) mode for γ $10^3(\eta_a$ 10^{21}Pa .s) to the SR mode for $\gamma > 6\times10^3(\eta_a < 6\times10^{20}$Pa .s), corresponding to a decrease in slab dip when increasing γ. A weaker upper-mantle in *Ribe* [2010] facilitates trench retreat and thus reduces the slab's dip. In contrast, in our models, the mean dip reduces with increasing mantle viscosity (η_a, i.e., low γ), and the slab folds in all cases. These contrasting results are explained by fundamental differences in our modeling assumptions. Indeed, while in free-subduction models the trench's displacements are only constrained by the slabs' properties, in our models the kinematic condition on the overriding plate plays a first-order role and consequently also controls the slab's mode of deposition [*Heuret et al.*, 2007; *Gibert et al.*, 2012].

With numerical models of free-subduction, *Stegman et al.* [2010] determined five "subduction" modes (which include the four previous deposition modes of *Schellart* [2008]), occurring within a range of about 4 orders of magnitude of a Stokes buoyancy (B_s $\Delta\rho ge/\eta_a$) and an effective flexural stiffness (defined as D^* γ/β^3). From their diagram, one can see for instance that upon decreasing the viscosity of the upper mantle, both B_s and D^* increase, and trench retreat is facilitated (regimes I, II, and IV). With our choices of parameters (see Table 2), our range of mantle viscosities provide a Stokes buoyancy B_s comprised between 5×10^{-14}s^{-1} and 5×10^{-13}s^{-1}, so that our models stand well out of the diagram of *Stegman et al.* [2010] (limited to $B_s \geq 10^{-12}$). Yet our trench always retreats and the slab always folds (which corresponds to the style 1a of *Gibert et al.* [2012]). In addition, *Stegman et al.* [2010] linked their slab deposition modes with an effective radius of curvature, which expression remains explicitly independent from the mantle's viscosity (their equation (10)). However, our results indicate that mantle viscosity exerts a first-order control on both the slab dip and the folding periodicity.

A more detailed comparison is hindered by our fundamentally different approach, all the more that it is not our aim here to vary the plates rigidity nor density (yet). In fact, *Gibert et al.* [2012] showed (in agreement with *Heuret et al.* [2007]) that kinematic conditions alone also determine four styles of slab deposition, yet with the abovementioned dimensionless numbers remaining fixed.

The folding cyclicity obtained with our models may more appropriately be compared with scaling analyses of a viscous sheet falling in a viscous fluid [*Ribe*, 2003]. First, *Ribe* [2003] provided a scaling law that distinguishes a "free folding" mode from a "forced folding" mode depending on the dimensionless number Π

$$\Pi = H\left(\frac{\Delta\rho g}{\eta V h^2}\right)^{1/4}, \tag{26}$$

where H is the effective fall height, $\Delta\rho g$ the sheet buoyancy, η its viscosity, V its velocity, and h its thickness. If $\Pi < 3.9$, then gravity can be neglected and slab folding belongs to the "forced mode." In our models, parameters are as follows: η η_p, V v_s 7.2cm .yr ^{1}, H $(H_{um}$ e$)/\sin(\theta)$, where θ is the slab dip and h e is the plate thickness. The only parameter that is not constrained is the slab dip, which changes through time except for mantle viscosities $>8\times10^{20}$Pa .s. But the scalings laws of *Ribe* [2003] were defined valid only when the surrounding fluid has negligible effects. In our models, we find that the mantle viscosity has negligible effects for $\eta_a \leq 10^{20}$Pa .s. We calculate that the minimum dip for which folding would be dominated by gravity is $\simeq 20°$, and we note that it is only episodically reached. On the other hand, the mean dip that we model for a mantle viscosity of 10^{20}Pa .s reaches about 30°, which gives Π 2.6. Therefore, we are in the "forced folding" mode. One would need to increase $\Delta\rho$ to 250kg .m ^{3} or reduce v_s to 1.4cm .yr ^{1} in order to have the system evolve to a "free-folding" mode.

Note that the Andean subduction zone might be a good example of a "forced-subduction," since the age of the Nazca plate from Northern Peru to Southern Chile is about 40 Myr on average, indicating that its buoyancy stands only slightly above neutral with respect to the upper mantle [*Afonso et al.*, 2007; *Gerbault et al.*, 2009]. Therefore, it is unlikely that the slab-pull alone drove the last ~40 Myr of subduction in the area (see *Martinod et al.* [2010] and *Somoza and Ghidella* [2005] for plate ages and reconstructions). Yet meanwhile, the second largest mountain belt in the world (the Altiplano) was built.

Having identified that our models stand in the "forced-folding" mode, we can now calculate the predicted amplitude (δ_b) and period (t_b) of viscous bukling according to *Ribe* [2003]

$$\delta_b = 0.5H, \qquad t_b = \frac{1.218H}{V}. \tag{27}$$

Inserting our parameters given above and with a mean slab dip equal to 30°, we obtain δ_b 570km and t_b 19.3Myrs . These predicted values are found consistent with our results, since our modeled folding period is close to 20 Myr for $\eta_a \leq 10^{20}$Pa .s, and our modeled fold width is about 500 km (Figure 9).

Lee and King [2011] and *Čížková and Bina* [2013] obtained similar values with numerical models accounting for temperature-dependent rheologies and either fixed or free trench motion. Although these studies have tested the effect of the slab strength and of the viscosity jump at the 660 km depth transition zone, they do not display the effect of mantle viscosity on folding cyclicity.

Further quantification of the controlling parameters on the dynamics of subduction, and more specifically the role of far-field boundary conditions with respect to the slab's relative viscosity and density, remains the subject of an upcoming study.

6.2. The Evolution of Slab Dip in the Andes

The Wadati-Benioff zone of the subducting Nazca plate under South America is observable down to about 250 km depth. Although beneath Ecuador and Bolivia the dip of the slab is about 30°, beneath Peru (3 15° S) and Central Chile/NW Argentina (27 33° S) horizontal subduction was identified [*Gutscher et al.*, 2000; *Espurt et al.*, 2008; *Marot et al.*, 2013], in association with a lack in Quaternary volcanism. Compilation studies of the distribution of igneous rocks, as well as geochemical, isotopic, and tectonic structures along the margin, reveal cyclic patterns of about 30–40 Myr, which have been linked with repeated slab flattening events [e.g., *Ramos*, 2009; *Haschke et al.*, 2006; *Martinod et al.*, 2010]. In turn, several mechanisms have been proposed to cause flat subduction:

1. Subduction of buoyant ridges or oceanic plateaus which seem to correlate with present-day zones of flat slabs [*Gutscher et al.*, 2000; *Espurt et al.*, 2008]. However, numerical studies by *Van Hunen et al.* [2002] and

Gerya et al. [2009] show that buoyant anomalies are not sufficient to form horizontal slabs. Moreover, many observed subducting ridges around the Pacific ring do not display flat slab segments [*Skinner and Clayton*, 2013].

2. Periodic slab break-off due to rheological weakening [e.g., *Billen*, 2010], leading to an upward rebound of the remaining slab [*Haschke et al.*, 2006]. Yet this scenario remains problematic as the Nazca slab becomes younger toward the South where no flat subduction is reported. An alternative is to consider a weak slab still submitted to slab-pull, which deforms by viscous stretching below the overriding plate [*Gerbault et al.*, 2009].

3. Corner flow in the asthenospheric wedge, by suction, would pull the subducted part of the plate up toward the base of the overriding plate. Recently, this hypothesis was fed by the modeling of cratonic roots beneath continents under which past segments of horizontal subduction are suspected [*O'Driscoll et al.*, 2012].

4. Metastability of the continental crust in the eclogite stability field [e.g., *Kay and Kay*, 1993; *Le Pichon et al.*, 1992; *DeCelles et al.*, 2009]. The catastrophic delamination of accumulated eclogitic material below an Andean magmatic arc has to be replaced either by warm incoming asthenosphere (as proposed by *Kay and Kay* [1993] for the Puna) or by the slab itself [*Ramos*, 2009; *DeCelles et al.*, 2009].

Without disregarding these mechanisms, here we argue for another scenario for shallow plate subduction, which is consistent with tomographic images in which subducted plates seem to lie on the 660 km depth transition zone [e.g., *Fukao and Obayashi*, 2013]. It also presents the advantage of tackling a large period of time. *Gibert et al.* [2012] proposed that slab folding over the 660 km depth discontinuity leads to periods of flat subduction. Nonetheless, their models produced shorter periods than those identified for the Andes. In the present work, we modeled cyclic periods consistent with those recorded in Andes, when using upper-mantle viscosities in between 3.10^{20}Pa .s and 5.10^{20}Pa .s. They correspond to values commonly found in the literature [*Karato and Wu*, 1993; *Billen*, 2010] but remain below other estimations [e.g., *Forte and Mitrovica*, 2001].

Our bilayered mantle viscosity models, in section 5.4, shows the effect of a lower viscosity layer from 90 to 200 km depth, producing similar results to those with an appropriate single viscosity. Thus, a sufficient temperature increase in the mantle can affect folding cycles and diminish slab dip. This is consistent with regional mantle hydration being able to diminish the viscosity and trigger horizontal subduction [*Manea et al.*, 2012]. We may also speculate that in earlier times, when the Earth was generally hotter, flat slabs would have been shorter, but more frequent.

6.3. How Slab Folding May Affect Convergence Rates in the Andes

Several authors have pointed out variations in the kinematics of the South American and Nazca plates. Both plates motions varied over the last 80 Myr [*Pardo-Casas and Molnar*, 1987; *Sdrolias and Müller*, 2006] with a peak in the convergence velocity about 25 Myr ago (at 15 cm/yr), which has been decreasing since [*Sdrolias and Müller*, 2006; *Somoza and Ghidella*, 2005]. Several interpretations have been proposed. One of them is the rupture of the Farallon plate [*Pardo-Casas and Molnar*, 1987]. But this hypothesis has not yet been supported by a numerical model.

Variations in the subduction velocity have been related by *Tetzlaff and Schmeling* [2009] to major phase transformations that occur as a slab goes through 410 and 660 km depths. However, the "parachute"-effect of metastable olivine in their thermal convection model leads to a time period of the order of 3–4 Myr, which is an order of magnitude less than the timing reported for the Andes. Recently, *Lee and King* [2011] and *Čížková and Bina* [2013] modeled buckling of stagnant slabs at the 660 km depth transition zone, accounting for the 410 km exothermic and 660 km endothermic phases transitions, and succeeded in generating variations in slab rollback velocity over periods of 20–40 Myr.

Quinteros and Sobolev [2013] developed numerical models assuming that a slab break-off had occurred prior to 25 Myr, so that their model begins with subduction initiation. These authors first applied a far-field plate convergence of $15 cm.yr^{-1}$, which they released as the slab progressively sank into the mantle, the slab being then only submitted to its own weight and mantellic resistance. This model fits well the data of decreasing plate convergence since 25 Myr (e.g., compiled by *Sdrolias and Müller* [2006]).

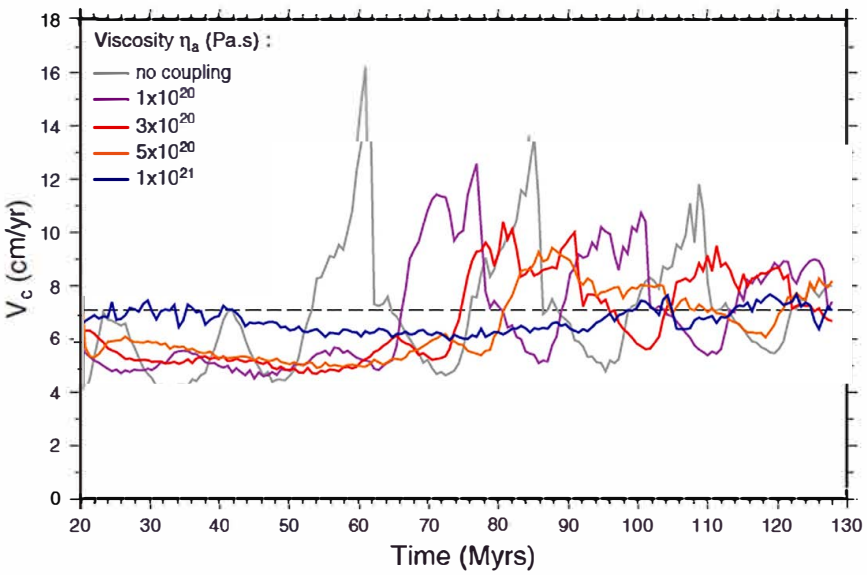

Figure 13. Temporal evolution of the convergence velocity for models with different viscosities of the isoviscous mantle, and for an applied far field convergence of 7 cm/yr.

Although this scenario is elegant, it relies on the primary assumption of a slab break-off that enables "resetting" of the subduction from 25 Myr. However, we are not aware of field evidences indicating a broad scale slab break-off all along the Central and South Andean margin at 25 Myr. We therefore propose alternatively, to look for an explanation of variations in the subduction velocity over a longer time period than 25 Myr (Andean subduction has been active for more than 100 Myr). Although our numerical approach accounts for much simpler assumptions than those of *Quinteros and Sobolev* [2013] (no temperature-dependent rheology, no phase transformation), our modeled process of cyclic slab folding every 30–40 Myr may provide a suitable explanation.

We cannot directly look at a self-consistent evolution of far-field plate motions, since we imposed them as constant during all the time duration of our models. However, we can follow the evolution of relative plate convergence (V_c) by looking at the speed of subduction at the trench. Figure 13 displays the temporal evolution of V_c for different mantle viscosities. Note that the first fold initiates between 50 and 70 Myr. For mantle viscosities lower than 5×10^{20} Pa .s, the maximum V_c decreases with time and displays cycles of the order of several cm/yr. However, for a given far-field plate convergence of 7cm .yr ^{1}, the maximum of 15cm . yr ^{1} reported for the Andean margin is never reached [*Pardo-Casas and Molnar*, 1987; *Sdrolias and Müller*, 2006]. An alternative might be to increase the applied far-field convergence rate to more than 7cm .yr ^{1}.

The driving force associated with far-field plate velocities competes with the resistance of the upper mantle to slab penetration on the long term. The higher the viscosity jump at the 660 km depth transition zone, the more it acts as a brake to continuous plate subduction, as demonstrated by *Quinteros and Sobolev* [2013]. The facts that (i) driving forces in play are limited by lithospheric strength and its ability to concentrate deformation and (ii) that stresses can efficiently transfer from 660 km depth to the top surface as shown here all together hint at the complex interplay between cyclic patterns in subduction dynamics and the evolution of far-field plate motions. Larger-scale models involving self-consistent mantle convection and yielding plates should better evidence this relationship in a near future [e.g., *Rolf et al.*, 2012; *Gerault et al.*, 2012].

Here we have shown on purpose the stress field within plates, and we note that this information is generally absent in other subduction modeling studies. The stresses involved in our 90 km thick visco-elastic plates implicate driving forces in the upper limit of those evaluated for the Earth (integration of 200 MPa from Figure 11 provides 1.8×10^{13} N.m). These boundary forces would be reduced by a factor four if plates were modeled half thinner (especially the oceanic plate) and half as strong. However, similarly high driving forces have been involved in the building of the Himalayas and the Altiplano since 30–40 Myr, which thus testifies of their importance in producing the Earth's tectonic structures. The other extreme point of view consisting

in accounting for weak plates and free plate boundaries (e.g., free-subduction) would not generate such significant mountain belts. Here we did not aim at testing the rheology of plates (elastic, viscous, and plastic) nor their thickness, for sake of paper length. However, *Gibert et al.* [2012] showed the effect of plate viscosity on folding cyclicity.

7. Conclusion and Prospects

We performed 2-D numerical experiments in which we proposed an alternative scenario for subduction cyclicity in the Andes, following *Gibert et al.* [2012]. However, *Gibert et al.* [2012] did not account for a viscous mantle, and a lower period of cycles was obtained in comparison to geological data along the Andes (20 Myr versus 40 Myr). Here we have developed a numerical solid-fluid coupling method which allows us to account for upper mantle viscosities within the commonly accepted range, and we obtained the consistent timing for a viscosity range of 3 5×10^{20} Pa .s.

Slab folding is associated with periodic flattening around 100–150 km depth and extends over several hundreds of kilometers, and we propose that this scenario may apply to Central Chile. Yet a more specific parametric study is necessary.

Differences in periods of cycles and slab dip might be explained by changes in upper mantle viscosity. The arrival of a thermal plume might affect the tectonics of a large region [e.g., *Burov et al.*, 2007], and the subduction of buoyant oceanic plateaus may also play a role [*Martinod et al.*, 2013], but it was not the objective of the present study to explore such effects. Variations in plate rheology and in far-field plate motion were also kept aside, since a number of combinations are possible and rely on data from a specific area. It remains necessary to combine kinematic boundary conditions with the rheological properties of the entire system in order to better assess the modes of slab deposition on the 660 km depth transition zone. Yet complementary and precise seismic tomography is also required.

This study is restricted to two dimensions and we believe that three-dimensional effects such as toroidal flow must be taken into account [e.g., *Morra and Regenauer-Lieb*, 2006; *Schellart*, 2004], especially in the context of the 5000 km long Andean margin. Folding periodicity might vary if the fluid is able to escape from the sides of the subducting panel. In addition, convergence between the Nazca and South American plates has been oblique for most of the time since 100 Ma [*Somoza and Ghidella*, 2005]. Obliquity cannot be grasped by a two-dimensional model. In order to tackle these mechanisms, the original method of fluid-solid coupling presented here is currently being implemented in three dimensions.

Acknowledgments
We thank H. Schmeling and an anonymous reviewer for their constructive comments and suggestions. We are particularly grateful to the Editor T. Becker whose advice greatly helped improving this manuscript. M. Marot is thanked for her careful checking of the English grammar. The numerical simulations were run on the University of Nice Sophia Antipolis CICADA cluster.

References

Afonso, J. C., G. Ranalli, and M. Fernandez (2007), Density structure and buoyancy of the oceanic lithosphere revisited, *Geophys. Res. Lett.*, *34*, L10302, doi:10.1029/2007GL029515.

Bellahsen, N., C. Faccenna, and F. Funiciello (2005), Dynamics of subduction and plate motion in laboratory experiments: Insights into the plate tectonics behavior of the earth, *J. Geophys. Res.*, *110*, B01401, doi:10.1029/2004JB002999.

Billen, M. I. (2010), Slab dynamics in the transition zone, *Phys. Earth Planet. Inter.*, *183*(12), 296 308, doi:10.1016/j.pepi.2010.05.005.

Bonnardot, M. A., R. Hassani, and E. Tric (2008a), Numerical modelling of lithosphere asthenosphere interaction in a subduction zone, *Earth Planet. Sci. Lett.*, *272*(34), 698 708, doi:10.1016/j.epsl.2008.06.009.

Bonnardot, M. A., R. Hassani, E. Tric, E. Ruellan, and M. Regnier (2008b), Effect of margin curvature on plate deformation in a 3 D numerical model of subduction zones, *Geophys. J. Int.*, *173*, 1084 1094.

Burov, E., L. Guillou Frottier, E. d'Acremont, L. Le Pourhiet, and S. Cloetingh (2007), Plume headlithosphere interactions near intra continental plate boundaries, *Tectonophysics*, *434*, 15 38, doi:10.1016/j.tecto.2007.01.002.

Burstedde, C., O. Ghattas, G. Stadler, T. Tu, and L. C. Wilcox (2009), Parallel scalable adjoint based adaptive solution of variable viscosity stokes flow problems, *Comput. Methods Appl. Mech. Eng.*, *198*, 1691 1700, doi:10.1016/j.cma.2008.12.015.

Capitanio, F., D. Stegman, L. Moresi, and W. Sharples (2010), Upper plate controls on deep subduction, trench migrations and deformations at convergent margins, *Tectonophysics*, *483*, 80 92, doi:10.1016/j.tecto.2009.08.020.

Cattin, R., H. Lyon Caen, and J. Chéry (1997), Quantification of interplate coupling in subduction zones and forearc topography, *Geophys. Res. Lett.*, *24*, 1563 1566, doi:10.1029/97GL01550.

Chéry, J., M. D. Zoback, and R. Hassani (2001), An integrated mechanical model of the San Andreas Fault in central and northern California, *J. Geophys. Res.*, *106*(B10), 22,051 22,066, doi:10.1029/2001JB000382.

Christensen, U. R. (1996), The influence of trench migration on slab penetration into the lower mantle, *Earth Planet. Sci. Lett.*, *140*, 27 39, doi:10.1016/0012 821X(96)00023 4.

Cízková, H., and C. R. Bina (2013), Effects of mantle and subduction interface rheologies on slab stagnation and trench rollback, *Earth Planet. Sci. Lett.*, *379*, 95 103.

Cízková, H., J. Van Hunen, A. P. Van den Berg, and N. J. Vlaar (2002), The influence of rheological weakening and yield stress on the interac tion of slabs with the 670 km discontinuity, *Earth Planet. Sci. Lett.*, *199*(34), 447 457, doi:10.1016/S0012 821X(02)00586 1.

Cundall, P. A., and M. Board (1988), a microcomputer program for modeling large strain plasticity problems, In: *Proceedings, 6th International Conference on Numerical Methods in Geomechanics, Innsbruck Austria*, edited by G. Swoboda, and AA. Balkema, pp. 2101 2108, Rotterdam, Netherlands.

DeCelles, P. G., M. N. Ducea, P. Kapp, and G. Zandt (2009), Cyclicity in cordilleran orogenic systems, *Nat. Geosci.*, *2*(4), 251 257, doi:10.1038/ngeo469.

Dohrmann, C. R., and P. B. Bochev (2004), A stabilized finite element method for the stokes problem based on polynomial pressure projections, *Int. J. Numer. Methods Fluids*, *46*(2), 18 201, doi:10.1002/fld.752.

Espurt, N., F. Funiciello, J. Martinod, B. Guillaume, V. Regard, C. Faccenna, and S. Brusset (2008), Flat subduction dynamics and deformation of the South American Plate: Insights from analog modeling, *Tectonics*, *27*, TC3011, doi:10.1029/2007TC002175.

Felippa, C. A., K. C. Park, and C. Farhat (2001), Partitioned analysis of coupled mechanical systems, *Comput. Methods Appl. Mech. Eng.*, *190*, 3247 3270.

Folguera, A., and V. A. Ramos (2011), Repeated eastward shifts of arc magmatism in the Southern Andes: A revision to the long term pattern of Andean uplift and magmatism, *J. South Am. Earth Sci.*, *32*(4), 531 546.

Forsyth, D., and S. Uyeda (1975), On the relative importance of the driving forces of plate motion, *Geophys. J. Int.*, *43*(1), 163 200, doi:10.1111/j.1365 246X.1975.tb00631.x.

Forte, A. M., and J. X. Mitrovica (2001), Deep mantle high viscosity flow and thermochemical structure inferred from seismic and geodynamic data, *Nature*, *410*(6832), 1049 1056, doi:10.1038/35074000.

Fukao, Y., and M. Obayashi (2013), Subducted slabs stagnant above, penetrating through, and trapped below the 660 km discontinuity, *J. Geophys. Res. Solid Earth*, *118*, 5920 5938, doi:10.1002/2013JB010466.

Funiciello, F., C. Faccenna, and D. Giardini (2004), Role of lateral mantle flow in the evolution of subduction systems: Insights from laboratory experiments, *Geophys. J. Int.*, *157*(3), 1393 1406, doi:10.1111/j.1365 246X.2004.02313.x.

Gerault, M., T. Becker, B. Kaus, C. Faccenna, L. Moresi, and L. Husson (2012), The role of slabs and oceanic plate geometry for the net rotation of the lithosphere, trench motions, and slab return flow, *Geochem. Geophys. Geosyst.*, *13*, Q04001, doi:10.1029/2011GC003934.

Gerbault, M., J. Cembrano, C. Mpodozis, M. Farias, and M. Pardo (2009), Continental margin deformation along the Andean subduction zone: Thermo mechanical models, *Phys. Earth Planet. Int.*, *177*(34), 180 205, doi:10.1016/j.pepi.2009.09.001.

Gerya, T. V., and D. A. Yuen (2003), Characteristics based marker in cell method with conservative finite differences schemes for modeling geological flows with strongly variable transport properties, *Phys. Earth Planet. Int.*, *140*(4), 293 318, doi:10.1016/j.pepi.2003.09.006.

Gerya, T. V., C. Fossati, D. Cantieni, and D. Seward (2009), Dynamic effects of aseismic ridge subduction: Numerical modelling, *Eur. J. Mineral.*, *21*(3), 649 661, doi:10.1127/0935 1221/2009/0021 1931.

Gibert, G., M. Gerbault, R. Hassani, and E. Tric (2012), Dependency of slab geometry on absolute velocities and conditions for cyclicity: Insights from numerical modelling, *Geophys. J. Int.*, *189*(2), 747 760, doi:10.1111/j.1365 246X.2012.05426.x.

Glowinski, R., T. W. Pan, and J. Periaux (1995), A Lagrange multiplier/fictitious domain method for the Dirichlet problem generalization to some flow problems, *Jpn. J. Ind. Appl. Math.*, *12*(1), 87 108, doi:10.1007/BF03167383.

Glowinski, R., T. W. Pan, T. Hesla, and D. Joseph (1999), A distributed Lagrange multiplier/fictitious domain method for particulate flows, *Int. J. Multiphase Flow*, *25*(5), 755 794, doi:10.1016/S0301 9322(98)00048 2.

Got, J. L., V. Monteiller, J. Monteux, R. Hassani, and O. P. (2008), Deformation and rupture of the oceanic crust may control growth of Hawaiian volcanoes, *Nature*, *451*, 453 456.

Guillaume, B., J. Martinod, and N. Espurt (2009), Variations of slab dip and overriding plate tectonics during subduction: Insights from analogue modelling, *Tectonophysics*, *463*(14), 167 174, doi:10.1016/j.tecto.2008.09.043.

Gutscher, M. A., W. Spakman, H. Bijwaard, and E. R. Engdahl (2000), Geodynamics of flat subduction: Seismicity and tomographic constraints from the Andean margin, *Tectonics*, *19*(5), 814 833, doi:10.1029/1999TC001152.

Haschke, M., A. Günther, D. Melnick, H. Echtler, K. J. Reutter, E. Scheuber, and O. Oncken (2006), Central and southern Andean tectonic evolution inferred from arc magmatism, in *The Andes*, edited by O. Oncken et al., pp. 337 353, Springer, Berlin.

Hassani, R., D. Jongmans, and J. Chéry (1997), Study of plate deformation and stress in subduction processes using two dimensional numerical models, *J. Geophys. Res.*, *102*(B8), 17, 951 17,965, doi:10.1029/97JB01354.

Heuret, A., and S. Lallemand (2005), Plate motions, slab dynamics and back arc deformation, *Phys. Earth Planet. Inter.*, *149*(12), 31 51, doi:10.1016/j.pepi.2004.08.022.

Heuret, A., F. Funiciello, C. Faccenna, and S. Lallemand (2007), Plate kinematics, slab shape and back arc stress: A comparison between laboratory models and current subduction zones, *Earth Planet. Sci. Lett.*, *256*(34), 473 483, doi:10.1016/j.epsl.2007.02.004.

Huc, M., R. Hassani, and J. Chéry (1998), Large earthquake nucleation associated with stress exchange between middle and upper crust, *Geophys. Res. Lett.*, *25*(4), 551 554.

Jarrard, R. D. (1986), Relations among subduction parameters, *Rev. Geophys.*, *24*(2), 217 284, doi:10.1029/RG024i002p00217.

Karato, S., and P. Wu (1993), Rheology of the upper mantle: A synthesis, *Science*, *260*(5109), 771 778, doi:10.1126/science.260.5109.771.

Kay, R., and S. M. Kay (1993), Delamination and delamination magmatism, *Tectonophysics*, *219*(13), 177 189, doi:10.1016/0040 1951(93)90295 U.

Lai, M. C., and C. S. Peskin (2000), An immersed boundary method with formal second order accuracy and reduced numerical viscosity, *J. Comput. Phys.*, *160*(2), 705 719, doi:10.1006/jcph.2000.6483.

Lallemand, S., A. Heuret, and D. Boutelier (2005), On the relationships between slab dip, back arc stress, upper plate absolute motion, and crustal nature in subduction zones, *Geochem. Geophys. Geosyst.*, *6*, Q09006, doi:10.1029/2005GC000917.

Lamb, S. (2006), Shear stresses on megathrusts: Implications for mountain building behind subduction zones, *J. Geophys. Res.*, *111*, B07401, doi:10.1029/2005JB003916.

Lee, C., and S. D. King (2011), Dynamic buckling of subducting slabs reconciles geological and geophysical observations, *Earth Planet. Sci. Lett.*, *312*, 360 370.

Le Pichon, X., M. Fournier, and L. Jolivet (1992), Kinematics, topography, shortening, and extrusion in the India Eurasia collision, *Tectonics*, *11*(6), 1085 1098, doi:10.1029/92TC01566.

LeVeque, R. J., and Z. Li (1994), The immersed interface method for elliptic equations with discontinuous coefficients and singular sources, *SIAM J. Numer. Anal.*, *31*, 1019 1044, doi:10.1137/0731054.

Li, Z. H., and N. M. Ribe (2012), Dynamics of free subduction from 3 D boundary element modeling, *J. Geophys. Res.*, *117*, B06408, doi:10.1029/2012JB009165.

Manea, V. C., M. Pérez Gussinyé, and M. Manea (2012), Chilean flat slab subduction controlled by overriding plate thickness and trench rollback, *Geology*, *40*, 35 38, doi:10.1130/G32543.1.

Marot, M., T. Monfret, M. Pardo, G. Ranalli, and G. Nolet (2013), A double seismic zone in the subducting Juan Fernandez Ridge of the Nazca Plate (32°S), central Chile, *J. Geophys. Res. Solid Earth*, *118*, 3462–3475, doi:10.1002/jgrb.50240.
Martinod, J., L. Husson, P. Roperch, B. Guillaume, and N. Espurt (2010), Horizontal subduction zones, convergence velocity and the building of the Andes, *Earth Planet. Sci. Lett.*, *299*(34), 299–309, doi:10.1016/j.epsl.2010.09.010.
Martinod, J., B. Guillaume, N. Espurt, C. Faccenna, F. Funiciello, and V. Regard (2013), Effect of aseismic ridge subduction on slab geometry and overriding plate deformation: Insights from analogue modeling, *Tectonophysics*, *588*, 39–55, doi:10.1016/j.tecto.2012.12.010.
Maury, B. (2001), A fat boundary method for the Poisson problem in a domain with holes, *J. Sci. Comput.*, *16*(3), 319–339, doi:10.1023/A:1012821728631.
Mégard, F. (1984), The Andean orogenic period and its major structures in central and northern Peru, *J. Geol. Soc.*, *141*(5), 893–900, doi:10.1144/gsjgs.141.5.0893.
Morra, G., and K. Regenauer-Lieb (2006), A coupled solid-fluid method for modelling subduction, *Philos. Mag.*, *86*(21–22), 3307–3323.
O'Driscoll, L. J., M. A. Richards, and E. D. Humphreys (2012), Nazca-South America interactions and the late Eocene-late Oligocene flat slab episode in the central Andes, *Tectonics*, *31*, TC2013, doi:10.1029/2011TC003036.
Pardo-Casas, F., and P. Molnar (1987), Relative motion of the Nazca (Farallon) and South American Plates since late Cretaceous time, *Tectonics*, *6*(3), 233–248, doi:10.1029/TC006i003p00233.
Peskin, C. S. (1972), Flow patterns around heart valves: A numerical method, *J. Comput. Phys.*, *10*(2), 252–271, doi:10.1016/0021-9991(72)90065-4.
Poliakov, A. N., and Y. Podladchikov (1992), Diapirism and topography, *Geophys. J. Int.*, *109*(3), 553–564.
Prevost, J. H. (1981), DYNAFLOW: A nonlinear transient finite element analysis program, Princeton Univ., Princeton, N. J. [Available at http://www.princeton.edu/dynaflow/.].
Quinteros, J., and S. V. Sobolev (2013), Why has the Nazca Plate slowed since the Neogene?, *Geology*, *41*(1), 31–34, doi:10.1130/G33497.1.
Ramos, V. A. (2009), Anatomy and global context of the Andes: Main geologic features and the Andean orogenic cycle, in *Backbone of the Americas: Shallow Subduction, Plateau Uplift, and Ridge and Terrane Collision*, edited by S. M. Kay, V. A. Ramos, and W. R. Dickinson, vol. 204, pp. 31–65, Geol. Soc. of Am. Mem., Boulder, Colo.
Ribe, N. M. (2003), Periodic folding of viscous sheets, *Phys. Rev. E*, *68*(3), 036305.
Ribe, N. M. (2010), Bending mechanics and mode selection in free subduction: A thin-sheet analysis, *Geophys. J. Int.*, *180*(2), 559–576.
Rolf, T., N. Coltice, and P. Tackley (2012), Linking continental drift, plate tectonics and the thermal state of the earth's mantle, *Earth Planet. Sci. Lett.*, *351–352*, 134–146, doi:10.1016/j.epsl.2012.07.011.
Rubie, D. C., and R. D. Van der Hilst (2001), Processes and consequences of deep subduction, *Phys. Earth Planet. Int.*, *127*(1–4), 1–7.
Saul'ev, V. K. (1963), On solution of some boundary value problems on high performance computers by fictitious domain method, *Siberian Math. J.*, *4*(4), 912–925.
Schellart, W. P. (2004), Kinematics of subduction and subduction-induced flow in the upper mantle, *J. Geophys. Res.*, *109*, B07401, doi:10.1029/2004JB002970.
Schellart, W. (2008), Kinematics and flow patterns in deep mantle and upper mantle subduction models: Influence of the mantle depth and slab to mantle viscosity ratio, *Geochem. Geophys. Geosyst.*, *9*, Q03014, doi:10.1029/2007GC001656.
Schmeling, H., et al. (2008), A benchmark comparison of spontaneous subduction models—Towards a free surface, *Phys. Earth Planet. Inter.*, *171*, 198–223, doi:10.1016/j.pepi.2008.06.028.
Schubnel, A., F. Brunet, N. Hilairet, J. Gasc, Y. Wang, and H. W. Green (2013), Deep-focus earthquake analogs recorded at high pressure and temperature in the laboratory, *Science*, *341*(6152), 1377–1380.
Sdrolias, M., and R. D. Müller (2006), Controls on back-arc basin formation, *Geochem. Geophys. Geosyst.*, *7*, Q04016, doi:10.1029/2005GC001090.
Shemenda, A. I. (1993), Subduction of the lithosphere and back arc dynamics: Insights from physical modeling, *J. Geophys. Res.*, *98*, 16,167–16,185, doi:10.1029/93JB01094.
Skinner, S. M., and R. W. Clayton (2013), The lack of correlation between flat slabs and bathymetric impactors in South America, *Earth Planet. Sci. Lett.*, *371–372*, 1–5, doi:10.1016/j.epsl.2013.04.013.
Sobolev, S. V., and A. Y. Babeyko (2005), What drives orogeny in the Andes?, *Geology*, *33*(8), 617–620.
Somoza, R., and M. E. Ghidella (2005), Convergencia en el margen occidental de américa del sur durante el cenozoico: Subduccin de las placas de nazca, faralln y aluk, *Asoc. Geol. Argent. Rev.*, *60*(4), 797–809.
Stegman, D. R., J. Freeman, W. P. Schellart, L. Moresi, and D. May (2006), Influence of trench width on subduction hinge retreat rates in 3-D models of slab rollback, *Geochem. Geophys. Geosyst.*, *7*, Q03012, doi:10.1029/2005GC001056.
Stegman, D., R. Farrington, F. Capitanio, and W. Schellart (2010), A regime diagram for subduction styles from 3-D numerical models of free subduction, *Tectonophysics*, *483*, 29–45, doi:10.1016/j.tecto.2009.08.041.
Steinmann, G., C. I. Lissón, A. Sieberg, and R. Stappenbeck (1929), *Geologie von Peru*, Winter, Heidelberg, Germany.
Tetzlaff, M., and H. Schmeling (2009), Time dependent interaction between subduction dynamics and phase transition kinetics, *Geophys. J. Int.*, *178*, 826–844.
Underwood, P. (1983), Dynamic relaxation (in structural transient analysis), in *Computational Methods for Transient Analysis*, pp. 245–265, North Holland, Amsterdam.
Van Hunen, J., A. P. Van den Berg, and N. J. Vlaar (2002), The impact of the South American plate motion and the Nazca Ridge subduction on the flat subduction below South Peru, *Geophys. Res. Lett.*, *29*(14), 1690, doi:10.1029/2001GL014004.
Wannier, G. H. (1950), A contribution to the hydrodynamics of lubrication, *Q. Appl. Math.*, *8*(1), 1–32.
Weidner, D. J., J. Chen, Y. Xu, Y. Wu, M. T. Vaughan, and L. Li (2001), Subduction zone rheology, *Phys. Earth Planet. Inter.*, *127*(1), 67–81.
Ye, T., R. Mittal, H. Udaykumar, and W. Shyy (1999), An accurate cartesian grid method for viscous incompressible flows with complex immersed boundaries, *J. Comput. Phys.*, *156*(2), 209–240, doi:10.1006/jcph.1999.6356.
Zlotnik, S., P. Díez, M. Fernández, and J. Vergés (2007), Numerical modelling of tectonic plates subduction using x-FEM, *Comput. Methods Appl. Mech. Eng.*, *196*(4144), 4283–4293, doi:10.1016/j.cma.2007.04.006.